Electrochemical Growth of Metal Nanomaterials

Student: Ting-Kai Huang   Advisor: Dr. Hsin-Tien Chiu

Institute of Applied Chemistry, National Chiao Tung University

Abstract

In this thesis, we developed surfactant-assisted electrochemical methods, including galvanic reduction and electrochemical deposition, to grow one-dimensional (1D) Cu and Au nanostructures on solid electrodes.

First, the single crystalline face-centered cubic phase (fcc) Cu nanobelts (NBs) were prepared by reacting $CuCl_{2(aq)}$ with $Al_{(s)}$ in an aqueous solution of CTAC (cetyltrimethylammonium chloride) and HNO_3. The Cu NB exhibited a high-quality ribbon-like nanostructure with a thickness less than 15 nm, a width of 30-150 nm, and a length up to 10 µm.

In the second section, Cu NBs with a small and uniform belt-width were grown directly on carbon electrodes by using electrochemical deposition. The average width, thickness and length of the NBs were about 50 nm, 20 nm and several tens of micrometers, respectively. The belt-width can be controlled by changing reactant concentration and electrical field applied. Cyclic voltammetric (CV) experiments showed that a Cu NB electrode grown by a reduction charge of 0.5 C on a substrate of 0.018 cm^2 enhanced glucose oxidation ability. For glucose sensing, the electrode exhibited a high sensitivity of 79.8 µA/mM and a low detection limit of 0.1 µM in amperometric detection.

In the third section, growth of arrays of pagoda-topped tetragonal Cu nanopillar (length: 1-6 µm, width: 150 ± 25 nm) with {100}-side faces on Au/glass is achieved

by a simple galvanic reduction of $CuCl_{2(aq)}$ by $Al_{(s)}$ in $DTAC_{(aq)}$. Field emission (FE) measurement shows that the Cu nanopillars can emit electrons (10 μAcm^{-2}) at a turn-on field of 12.4 $V\mu m^{-1}$ with a calculated field enhancement factor β of 713.

Finally, this surfactant-assisted galvanic reduction was extended to grow directly Au nanothorns and nanourchins on Si. Nanothorns and nanourchins were prepared by reacting $HAuCl_{4(aq)}$ with $Sn_{(s)}$ in the presence of only $NaNO_{3(aq)}$ and both $CTAC_{(aq)}$ and $NaNO_{3(aq)}$, respectively, which were important to the product morphology development. FE measurements reveal that they have different FE performances based on their morphologies. Among them, Au nanourchins grown at 18 h exhibited the best FE efficiency (turn-on-field 6.3 $V\mu m^{-1}$, β 1150) because they protrude radially high aspect ratio (20-30) nanowires.
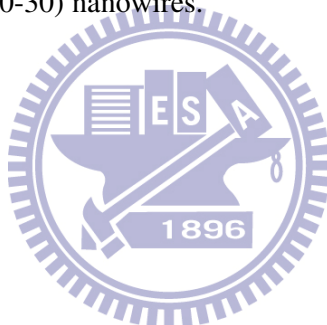
電化學法成長金屬奈米材料

研究生: 黃亭凱　　　　　　　　　　　　指導教授: 裴性天 博士

國立交通大學應用化學所

摘要

在本論文中，我們發展界面活性劑(烷基三甲基氯化銨)輔助電化學法，包含賈凡尼還原法與電化學沉積法，成功地成長銅與金一維奈米結構於電極上。

首先，我們利用氯化銅與金屬鋁的賈凡尼自發性氧化還原反應，在含有十六烷基三甲基氯化銨與硝酸的水溶液中成長單晶銅奈米帶。奈米帶帶厚小於 15 nm，帶寬範圍為 30-150 nm，長度可達 10 μm.

第二部份，我們利用電化學沉積法直接成長銅奈米帶於碳電極上。奈米帶平均帶寬為 50 nm，帶厚約 20 nm，長度可達數 10 μm。改變反應物濃度與施加電位可調控奈米帶帶寬。循環伏安實驗展示銅奈米帶電極(電沉積量 0.5 C，幾何面積 0.018 cm^2)具有增強電催化葡萄糖氧化的能力。在葡萄糖安培法感測中，此電極展現高靈敏度(79.8 μA/mM) 與低偵測極限(0.1 μM)。

第三部份為十二烷基三甲基氯化銨輔助賈凡尼還原法成長似寶塔蓋頂的四方形銅奈米柱陣列於金電極上。奈米柱四個長邊為{100}晶面構成，奈米柱長範圍為 1-6 μm，寬為 150 ± 25 nm。場發射量測顯示銅奈米柱陣列在 turn-on field 12.4 V μm^{-1} 有 10 μA cm^{-2} 電流密度且增強因子β 為 713.

最後部分，我們延伸界面活性劑輔助賈凡尼還原法直接成長金奈米錐與海膽結構於矽基材上。比較不同奈米結構對場發射性質的影響，實驗結果顯示奈米錐與奈米海膽都具有場發射性質，尤其反應十八小時的奈米海膽結構具高長寬比的奈米線(線徑 50-100 nm, 線長 1-3 μm, 長寬比 20-30)，展現最佳的場發射效能

(turn-on field 6.3 Vμm^{-1}, β 1150)。

Acknowledgments

Contents

Contents of Tables and Schemes

Chapter 1

Chapter 2

Chapter 3

Chapter 4

Chapter 5

List of Figures

Chapter 1

Introduction

1.1 Introduction

Recently, copper has been an excellent material for IC interconnects in microelectronic industry due to its low electrical resistivity, high electro-migration resistance, and good thermal conductance relative to aluminum.[1] Its good electrical and catalytic properties also employ as chemical catalyst and catalytic electrodes in organic syntheses and electro-catalytic reactions.[2-5] Therefore, the exploration of copper is still an important subject in modern science and engineering.

One-dimensional (1-D) nanostructures are materials constrained in two dimensions to less than 100 nm. Within this category of nanomaterials, researchers discriminate between nanorods (NRs) with aspect ratios (length/diameter) less than 10, nanowires (NWs) with aspect ratios greater than 10, and nanotubes (NTs) with hollow interiors.[6, 7] Research on nanostructures is primarily guided by three questions: (i) how can we produce large quantities of nanostructures with controllable sizes and shapes; (ii) what are the size- and shape-dependent physical and chemical properties of nanostructures; and (iii) how can the properties unique to nanostructures be exploited for applications? Pursuing answers to these questions has evolved into an active field of research now commonly referred to as nanoscience and nanotechnology.

1D nanomaterials have attracted intensive attention due to their unusual chemical and physical properties associated with the size and shape.[8] Based on them, many researches have demonstrated that single one or arrays of 1D nanomaterials used as a building block in electronic, photonic, and sensing devices, which could attain miniaturization and enhance the

performance. Among them, metal nanomaterials displaying surface plasmon resonance (SPR),[9] surface-enhanced Raman scattering (SERS),[10] and electrochemical catalytic properties become a popular research subject. However, until now, there have been few reports regarding direct growth of 1D metal nanomaterials on hard electrodes and their potential application.

In this dissertation, novel metal nanostructures, such as Cu NBs, tetragonal nanopillars, Au nanothorns and nanourchins, that fabricated by surfactant assisted electrochemical methods, were revealed. Their shape dependent electrochemical catalysis and electron field emission (FE) performance will be explored.

1.2 Properties and Application of Metal Nanomaterials

1.2.1 Surface Area Effect

The high specific surface area is one of important characteristics of the nanostructures. The population of the atoms at the surfaces increases extremely as the dimension decreases. In order to compare to the influence of the morphology on surface areas, we estimated surface area ratios of NB, NW and nanoparticle (NP) to a bulk cube (1 mm^3) as functions of corresponding geometric variables. Total amount of each nanostructure is equal to that of the bulk cube. As shown in Figure 1.1, the surface area of each nanostructure with comparable dimensions under 70 nm is at least 10,000 times larger than that of bulk cube. Interestingly, calculations show that NBs possess surface areas higher than NPs and NWs with comparable dimensions over 40 nm.

Although the surface area of NPs increases obviously as the diameter reduces from 40 nm, serious aggregation could happen and cause passivation of active sites in the process of crystal growth. On the other hand, the growth of 1D nanostructures and the formation of three-dimensional architectures on flat substrates increase the surface areas. This may boost the charge transfer happening between the interface of electrodes and species in solution.
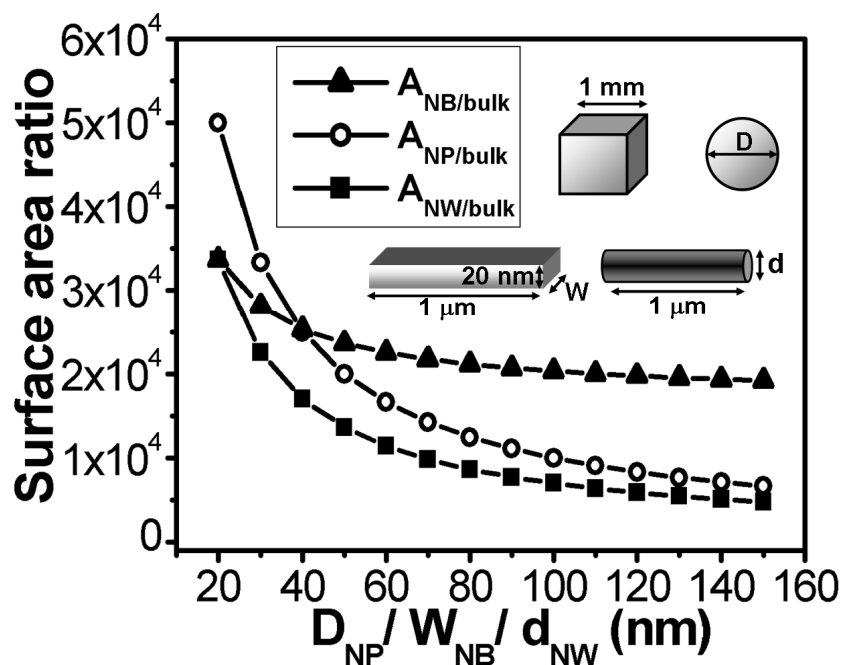
Figure 1.1 Comparison of estimated surface area ratios of NB, NW and NP to a bulk cube (1 mm^3) as functions of corresponding geometric variables: W_{NB} (NB width, ▲), d_{NW} (NW diameter, ■), and D_{NP} (NP diameter, ○). Total amount of each nanostructure is equal to that of the bulk cube.

1.2.2 Adsorption and Catalytic Property

As mentioned above, nanomaterials display high surface-area-to-volume ratios. It means that most atoms expose to uncoordinated sites and stand under unstable states. It is required to passivate these active sites by adsorbing atoms or molecules at the surface. Hence, strong adsorption behavior and high active sites are important features of nanomaterials.

Heterogeneous catalysis is a common technique in the chemical industry. It can synthesize various chemicals and reduce production cost. Metal nanoclusters have been long used as heterogeneous catalyst in synthetic organic compounds. Solid supported palladium nanoclusters are a typical example.[11] They can be employed in carbon-carbon coupling reaction, such as Suzuki Miyaura Cross-Coupling, Heck reaction and Stille coupling. Many

studies also showed Pd NPs displayed high catalytic efficiency for hydrogenation of alkene and oxidation of carbon monoxide. These properties were contributed to their excellent adsorption ability and high surface area.

Cu is a common catalyst because its abundance and chemical activity. In the syntheses of organic compounds, Cu NPs can catalyze the cyclization of Schiffs' bases and condensation of iodo-benzene to biphenyl.[2, 3] Besides, it can be used as a catalytic electrode for speeding up electro-reduction of oxygen and carbon dioxygen.[4, 5] These interesting properties involving energy and environment issues have attracted intense attention on the possible usage of Cu.

1.2.3 Electrochemical Property and Sensing

Electrochemical reactions taking place at the interface between flat electrodes and electrolyte solutions are often impeded by diffusion process. Recent development of nanotechnology has promoted the fabrication of nanostructured electrodes with the high roughness (ratio of real surface area to geometric area). These electrodes display high electrochemical active surface areas and accelerate the electrochemical reaction.

NP-modified electrodes, such as copper, gold, silicon and platinum NP electrodes, used as excellent electron transfer mediators, were known examples.[12-15] In recent years, 1D nanostructures have become interesting building blocks for constructing highly sensitive electrodes. Carbon nanotube (CNT), Pt NT, and Cu_2O NW electrodes have been demonstrated to be able to increase electro-oxidation ability of glucose and enhance the sensitivity for glucose detection.[16-18] Besides, mesoporous and macroporous Pt electrodes also displayed the same electrocatalytic ability.[19, 20] These designs of electrodes with high roughness increased undoubtedly high electro-catalytic active sites and boosted the kinetic-control reaction.

The morphologic effect of nanostructures on electrocatalytic activity is an important subject in material science. Each shape is correlated with which crystallographic facets exposed in the crystal. For example, three Pt electrodes, including (100), (110) and (111) single crystal,

displayed the different oxidation ability of hydrogen.[21] Wang et al. synthesized the monodispersed Pt nanocubes, which are consistent of six {100} family planes. Compare to Pt NPs, they enhanced catalysis for oxygen reduciton.[22] The morphology dependent electrochemical properties have started attracting more and more attention.

Cu NP electrodes could be used as catalytic electrodes for speeding up electro-reduction of oxygen and carbon dioxygen.[4, 5] They could be employed as sensing electrodes for glucose, diphenol and amino acid.[12, 23, 24]

1.2.4 Surface Plasmon Resonance (SPR) Absorption

The study of the colors of metal NPs can be traced back to 19th century when Michael Faraday synthesize colloidal solutions of gold exhibiting colours ranging from ruby red to amethyst.[25, 26] The various colors resulted from the surface plasmon band (SPB), which is a phenomenon observed in transmission, due to the presence of NPs, in solution or in the solid phase. For a special domain of frequency, NPs interact with incident light, resulting in a global scattering of it. This macroscopic feature can be explained by the collective resonance of the conduction electrons of the NP. A NP can be seen as an immobile and periodical cationic network in which a cloud of conducting electrons move. The latter are usually considered as free electrons.

Mie presented an analytical solution to Maxwell's equations which describe a isolated spherical particle in 1908.[27] Over the last three decades several numerical methods based on finite elements have been developed for overcoming the limitation in calculations of particles with arbitrary shape and multicomposition.[28] Among those the discrete dipole approximation (DDA) has been proven to be an effective method for estimating the optical properties of metal particles in nanoscale.[29] In most cases the extinction spectra of metal NPs under different conditions were simulated by the DDA method and compared with the experimental results.[30] The investigation of the influence of particle shapes on surface SPR wavelengths

was also performed

The particle shape and size are an important factor to the SPR wavelength, and many papers concerning the size effect of the spherical nanoparticles have been published.[31] Naturally, geometrical parameters also have strong influences on the SPR peaks, for example, triangle nanoplates. Schatz and co-workers have demonstrated that the increase of the side length of triangle nanoplates could lead their SPR peak to red shift by several hundred nanometers.[32]

This controllable optical property in terms of wavelength is quite exciting and interesting, and it enables the particles to be applied in biological sensing and drug delivery.[33] Because the photons with near-IR wavelengths can harmlessly pass through biological tissues, nanoplates with high extinction coefficients at the target tissues will convert the near-IR photons to heat at high yields. So they can be used in photothermal cancer therapy and photothermally triggered drug release.

1.2.5 Surface-enhanced Raman Scattering (SERS)

The change in wavelength that is observed when a photon undergoes Raman scattering is attributed to the excitation (or relaxation) of vibrational modes of a molecule. Because different functional groups have different characteristic vibrational energies, every molecule has a unique Raman spectrum. In accordance with the Raman selection rule, the molecular polarizability changes as the molecular vibrations displace the constituent atoms from their equilibrium positions. The intensity of Raman scattering is proportional to the magnitude of the change in molecular polarizability. Thus, aromatic molecules exhibit more intense Raman scattering than aliphatic molecules.

Even so, Raman scattering cross sections are typically 14 orders of magnitude smaller than those of fluorescence; therefore, the Raman signal is still several orders of magnitude weaker than the fluorescence emission in most cases. Because of the inherently small intensity of the Raman signal, the sensitivity limits of available detectors, and the intensity of the excitation

sources, the applicability of Raman scattering was restricted for many years.

In 1977, Jeanmaire and Van Duyne demonstrated that the magnitude of the Raman scattering signal can be greatly enhanced when the scatterer is placed on or near a roughened noble-metal substrate.[34] Strong electromagnetic fields are generated when the localized surface plasmon resonance (LSPR) of nanoscale roughness features on a silver, gold, or copper substrate is excited by visible light. When the Raman scatterer is subjected to these intensified electromagnetic fields, the magnitude of the induced dipole increases, and accordingly, the intensity of the inelastic scattering increases. This enhanced scattering process is known as surface-enhanced Raman (SER) scattering—a term that emphasizes the key role of the noble metal substrate in this phenomenon.

SER spectroscopy (SERS) can be exploited for sensitive and selective molecular identification. Recently, SERS has been used extensively as a signal transduction mechanism in biological and chemical sensing. Examples are trace analysis of pesticides, anthrax[35], prostate-specific antigen[36], glucose[37, 38], and nuclear waste[39]. SERS has also been implemented for identification of bacteria[40], genetic diagnostics[41], and immunoassay labeling[42-44]. A miniaturized, inexpensive, and portable SERS instrument makes the technique practical for trace analysis in clinics, the field, and urban settings[45].

1.2.6 Electron Field Emission (FE) Property

1D nanomaterials have a potential application as electron emitters in flat panel displays.[46] The FE of electrons under applied electric fields is a quantum-mechanical phenomenon which can be understood as a tunneling process across the energy barrier between the vacuum and the emitter. In general, Fowler–Nordheim (F-N) equation is used to describe field emission characteristics of metals,[47] which is expressed as $J = A(\beta^2 E^2/\Phi)\exp(-B\Phi^{3/2}/\beta E)$, where J is the current density, E the applied field, Φ the work function of the metal, β the field enhancement factor, indicating the degree of field emission enhancement by the tip shape of the

7

electron-emitting edge, and A and B are constants. According to the equation, the F-N plot, $\ln(J/E^2)$ versus $1/E$, is expected to be a straight line.

In recent years, there are some researches demonstrating that metal NW arrays display FE properties with low threshold voltages and high enhancement factors.[48, 49] It could be contributed to their high aspect ratio and good electrical conductance. Kim et al. further fabricated a FE display device of Cu NW arrays grown by chemical vapor deposition (CVD).[50] These revealed that metal NWs are promising candidates as FE electron sources.

1.3 Synthetic Approaches to Novel Nanostructures of Metals

In order to study systematically unusual properties of nanostructures correlated with geometric shapes and dimensions, researchers have developed some methods to fabricate diverse and uniform nanostructures. Based on the reaction systems and employed technique, these methods were divided into three types: First one is Direct Hard Template Methods; Second one is Self-assembly Micelle and Capping Reagent Methods of Surfactants, and the last is Vapor-Solid Phase Reaction. We will introduce them with graphs summarized below.

1.3.1 Direct Hard Template Methods

Figure 1.2 shows typical hard template-assisted methods, which is a simple way for fabricating 1D nanosructures.[6] General templates involve in inorganic solid materials and organic molecules or polymer. The former includes anodic aluminum oxide (AAO), highly oriented pyrolytic graphite (HOPG) with step edge surface and inorganic 1D nanomaterials. The latter contains polystyrene (PS) nanosphere arrays, porous polycarbonate and DNA biomolecules. These templates used as frameworks are filled or coated with desired materials and then removed by physical or chemical etching. Array of patterned nanodot or high-aspect-ratio NWs are known examples. The advantages of these methods are easily
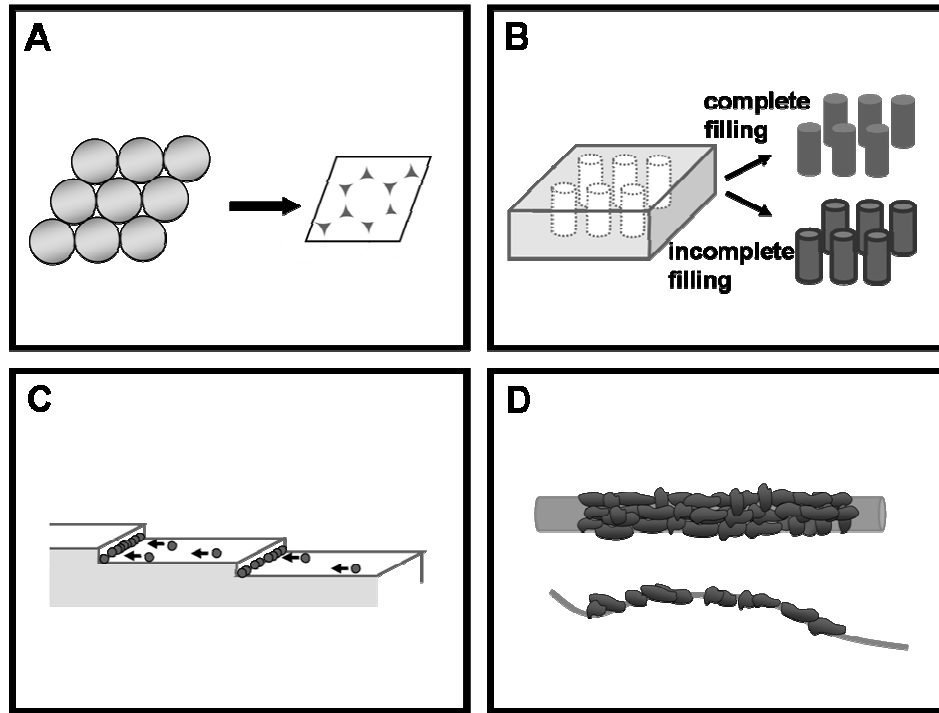
Figure 1.2 Four typical methods for controlling nanostructures. (A) Nanosphere array lithography; (B) porous template method; (C) step-edge surface method; (D) 1D nanomaterial template method.

controllable in product morphologies, low cost and reproducible. However, the drawback of complicated prefabrication and removal of templates existed. Four typical hard template methods shown in Figure 1.2 would be illustrated below.

1.3.1.1 Nanosphere array lithography

Nanosphere array lithography is an excellent method for fabricating regular tetragonal nanoparticle arrays. The PS nanoshpere colloids are dropped on a flat glass substrate. After evaporation of solvent, nanospheres self-assemble into a close-packing monolayer, as shown in Figure 1.2A. The arrays with the area of several millimeters could be used as a mask and coated with Ag by thermal evaporation. Ag nanoparticle arrays were formed after removal of nanosphere arrays.[51] The uniformity of the size displays well-defined SPR peaks and

possessed potential application for biosensing.

1.3.1.2 Porous Materials

Porous template-assisted methods are an often used technique. Among porous templates, AAO has become the most general hard template because of controllable pore diameter and length and high porous density. Figure 1.2B shows the strategy for achieving 1D nanostructures by using AAO templates. NWs and NTs can be formed by full and part filled channels with desire materials, respectively.[52, 53] For example, Gao et al. has employed AAO-assisted electrochemical deposition to fabricate Cu NW arrays.[54, 55] Qie et al. successfully prepared Cu NTs by AAO-templated electroless deposition.[56]

1.3.1.3 Step-edge Surface Substrates

Figure 1.2C illustrates fabrication of NWs using highly oriented pyrolytic graphite (HOPG). Penner et al. found that metal ions favor nucleation and growth along the HOPG step edge. Therefore, they grew Cu and Ag NW arrays on HOPG surfaces by electrochemical deposition.[57]

1.3.1.4 1D Nanomaterials and Biomolecules

Figure 1.2D depicts that 1D nanomaterials are employed as templates to synthesize coaxial NWs. Day et al. have fabricated Ag coated carbon NTs by carbon NT-templated electrochemical deposition.[58] Wolley et al. used DNA molecules with negative charges to attract Cu ions. Once reducing agent was added, Cu NPs would be formed and connected to form Cu NWs.[59, 60]

We summarize the direct hard template methods reported previously in Table 1.1.

1.3.2 Self-assembly Micelle and Capping Reagent Methods of Surfactants

Table 1.1 Direct template methods

Metal	Shape	Dimension (D diameter; W width; T thickness; L length)	reactant	Fabrication technique	Reaction condition (For example, template, system, additives, temperature)	Ref
Ag	Tetragonal particle	T 52 nm; L 100 nm	$Ag_{(s)}$	Nanosphere array lithography	PS nanosphere arrays, thermal coating	51
Cu	Wire	D 60 nm; L 30μm	$CuSO_{4(aq)}$	Porous template method	AAO, electrodeposition, electrolyte ($H_3BO_{3(aq)}$/ $H_2SO_{4(aq)}$)	54, 55
Cu	Tube	D 300 nm	$CuSO_{4(aq)}$		AAO, electroless deposition, electrolyte (sodium tartrate$_{(aq)}$/ $NaOH_{(aq)}$)	56
Ag	Wire	D 180-400 nm; L 30μm	Commercial plating solution		AAO, electrodeposition	52
Ag	Helical wire	D~10 nm	$AgNO_{3(aq)}$		AAO, electrodeposition、electrolyte ($H_3BO_{3(aq)}$)	53
Cu	Wire	D70-340 nm; L>10μm	$CuSO_{4(aq)}$	Step-edge surface template	Graphite, electrodeposition、electrolyte ($Na_2SO_{4(aq)}$)	57
Ag	Wire	D70-340 nm; L>10μm	$Ag_2SO_{4(aq)}$		Graphite, electrodeposition、electrolyte ($Na_2SO_{4(aq)}$ / saccharine$_{(aq)}$)	57
Ag	Wire	D 60 nm; L 30μm	$AgNO_{3(aq)}$	1D nanomaterial template	CNT, electrodeposition、electrolyte ($KNO_{3(aq)}$)	58
Cu	Wire	D 3 nm	$Cu(NO_3)_{2(aq)}$/ ascorbic acid$_{(aq)}$	Bio-molecule template	DNA	59
Ag	Wire	D 30-50 nm	$AgNO_{3(aq)}$/ hydroquinone$_{(aq)}$		DNA	60

11

There are three indispensable components, metal salts, reducing agents and stabilizers in solution phase synthetic methods. Stabilizers, such as surfactants are important reagents not only for avoiding NP aggregation and directing anisotropic growth of nuclei. These methods have synthesized many nanomaterials, including nanocubes (NCs), NRs, NWs and triangular nanoplates (NPs). Based on difference of additives and fabrication procedures, they could be divided into five types, including self-assembly micelle, capping reagent, seed-mediated growth, polyol methods, galvanic reduction and hydrothermal methods.
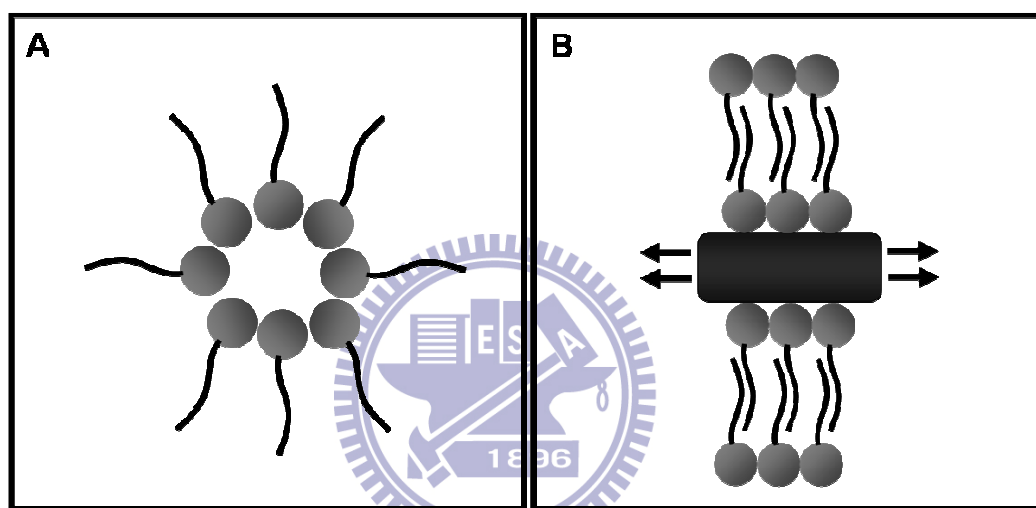
Figure 1.3 (A) self-assembled reverse micelle and (B) capping reagent mechanism of surfactants.

1.3.2.1 Micelle and Reverse Micelle Methods

This method, also called soft template method, is the early fabrication method of NPs. Surfactants have both hydrophilic and hydrophobic terminals and self-assemble into reverse micelles with various shapes in aqueous solution, as shown in Figure 1.3A. Nanocrystals are formed by reducing metal ions in this microreactor and stably dispersive in solution. Pileni et al. used rod-shape reverse micelles of AOT (sodium bis(2-ethylhexyl) sulfosuccinate) as soft templates in de-ionized water/ isooctane/ a trace of Cl$^-$ and synthesized Cu NRs.[61]

1.3.2.2 Seed-Mediated Growth

Murphy and coworkers have developed seed-mediated growth to fabricate and control 1D metal nanomaterials. When adding seeds into the mixture of metal salts, weak reducing agents and surfactants, the reaction would be activated and metal atoms could deposit selectively on the seeds to form anisotropic growth. NRs and NWs with an uniform diameter and aspect ratio were fabricated in the presence of 4 nm Ag seeds, $AgNO_3$/ ascorbic acid growth solution and cetyltrimethylammonium bromide (CTAB).[9] Figure 1.3B depicts that bilayer structures of surfactants (CTAB) self-assemble adsorbed selectively on specific crystal facets and confine their growth. The relatively fast growth rate of uncapped sites caused formation of NRs or NWs. CTAB, called capping reagents, played an important role for controlling anisotropic crystal growth.

1.3.2.3 Polyol Methods

Polyols, which are high-boiling-point solvents and weak reducing agents, were used early for fabrication of metal and alloy colloid particles. When raising reaction temperature, polyol could increased the solubility of metal salt and reducing force. It is a convenient method to control the rate of nucleation and growth by adjusting reaction temperature. Xia and coworkers fabricated Ag NCs using ethylene glycol as a solvent and a reducing agent and adding $AgNO_3$ and poly(vinyl pyrroli-done) (PVP) into thermal reflux reaction system.[62, 63] Characterizations of infrared and X-ray photoelectron spectra confirmed that PVP, which adsorbed on Ag nanocrystal surfaces by O and N atoms, played the role of the capping reagent.[64]

1.3.2.4 Galvanic Displacement Reduction

A little different from typical homogeneous solution reaction system mentioned above, we evolved heterogeneous galvanic displacement reduction to fabricate Cu and Ag NBs, as

shown in Figure 1.4.[65] Sacrificial metals oxidized itself and reduced the another metal ions at the interface of metal and solution. In general, fractal or dendrites would grow without any additives. We found that the products could be controlled to regular 1D nanostructures in the
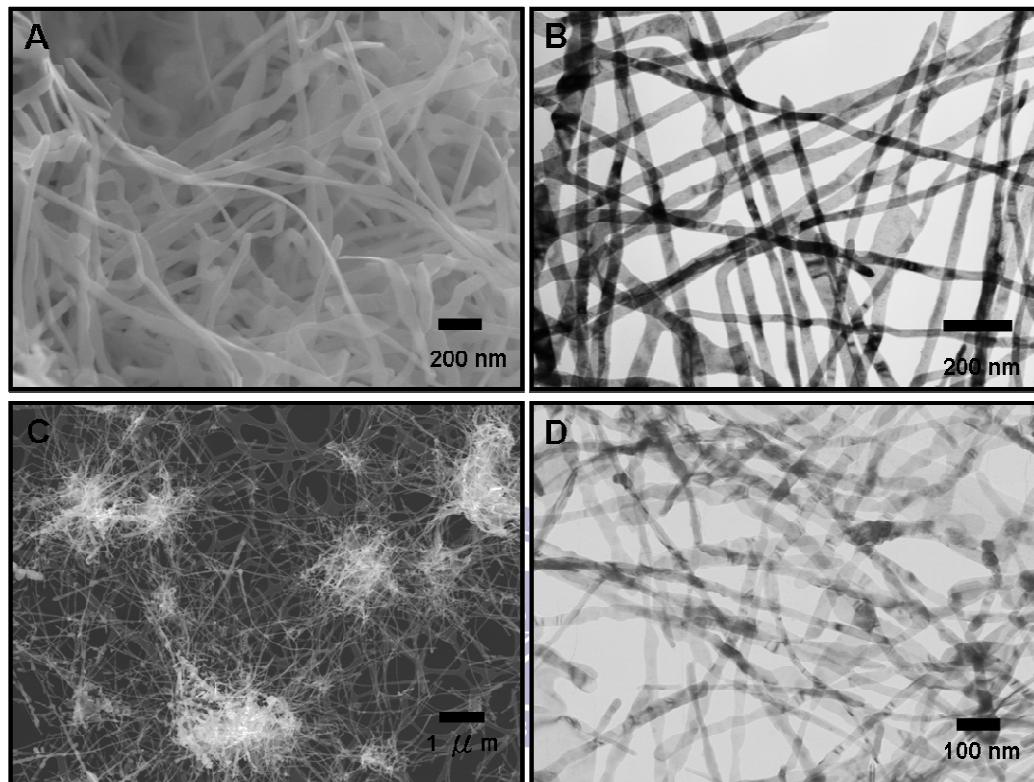
Figure 1.4 (A) SEM and (B) TEM mages of Cu NBs grown on Al TEM grid; (C) SEM and (D) TEM mages of Ag NBs grown on Cu TEM grid.

presence of CTAC surfactant and inorganic acid. It is an excellent approach to grow and immobilize the diverse nanostructures on electrodes simultaneously. Multiple potential application such as sensing electrodes or SERS substrates could be expected.

1.3.2.5 Hydrothermal Methods

The autoclave is a common used reactor which can provide high pressure reaction condition under high temperature. Several literatures reported that it is possible to synthesize NWs in the presence of additives of small molecules or polymer surfactants as capping reagents. Liu,

Table 1.2 Self-assembly Micelle and Capping Reagent Methods of Surfactants

Metal	Shape	Dimension (D diameter; W width; T thickness; L length)	Reactant	Fabrication technique	Reaction condition	Ref
Cu	Rod	D 5 nm; L 30 nm	$Cu(AOT)_2$/ N_2H_4	Micelle, reverse micelle	\water/ isooctane/ trace Cl^-	[61]
Ag	Rod, wire	D_{rod} 10-20 nm; L_{wire} 2-4μm	$AgNO_{3(aq)}$/ ascorbic acid$_{(aq)}$	Seed-assisted method	Ag seed (4 nm)/ CTAB/ NaOH	[9]
Ag	Cube	~D 80 nm	$AgNO_3$/ ethylene glycol	Polyol method	PVP/ 433 K	[63]
Ag	Wire	D 30-40 nm; L 50μm	$AgNO_3$/ ethylene glycol		Pt seed/ PVP/ 433 K	[62 64]
Cu	Belt	W 30-150 nm; T <15nm; L up to10-40μm	$CuCl_{2(aq)}$/ $Al_{(s)}$	Galvanic reduction	CTAC/ HNO_3	[65]
Ag	Belt	W30-100 nm; T <10nm; L up to 10μm	$AgNO_{3(aq)}$/ $Cu_{(s)}$		CTAC	[65]
Cu	Wire	D ~85 nm; L~μm	$CuSO_{4(aq)}$/ $H_3PO_{3(aq)}$	Hydrothermal method	glycerol/ SDBS/ NaOH / autoclave/ 393 K	[66]
Cu	Wire	D 90-120 nm; L 40-50 μm	$Cu(NO_3)_{2(aq)}$/ $N_2H_{4(aq)}$		ethylenediamine/ NaOH/ 333 K	[67]
Cu	Wire	D 30–100 nm; L ~mm	$CuCl_{2(aq)}$ / octadecylamine$_{(aq)}$		Autoclave/ 393- 453 K	[68]
Cu	Cable	D_{core} 80 nm; D_{sheath} 200 nm	$CuCl_{2(aq)}$/ $PVA_{(aq)}$		NaOH/ autoclave/ 473 K	[71]
Ag	Wire	D 100 nm; L up to 500 mm	$AgNO_{3(aq)}$/ glucose		NaCl/ autoclave/ 453 K	[69]
Ag	Wire	D 30 nm	$AgNO_{3(aq)}$/ methenamine$_{(aq)}$		gemini surfactant 16-3-16/ autoclave/ 373 K	[70]

Ag	Cable	D_{core}150-200 nm; L 100 μm	$AgNO_{3(aq)}$/ $PVA_{(aq)}$		autoclave / 433 K	72
Ag/C	Cable	D 200-250 nm; L 10 μm	$AgNO_{3(aq)}$/ α-D-glucose or β-cyclodextrine		autoclave / 433 K	73

Abbreviation

AOT= sodium bis(2-ethylhexyl)sulfosuccinate

CTAB= cetyltrimethylammonium bromide

PVP= poly(vinyl pyrrolidone)

CTAC= cetyltrimethylammonium chloride

SDBS= sodium dodecyl benzenesulfonate

gemini surfactant 16-3-16= 1,3- *bis*(cetyldimethylammonium) propane dibromide

PVA= poly(vinyl alcohol)

Chang, Shi, Wang and Xu et al. fabricated a large amount of ultra-long Cu and Ag NWs by this method.[66-70] Yu et al. used poly(vinyl alcohol) (PVA) as a reducing agent and a capping reagent and synthesized PVA coated Cu and Ag nanocables.[71, 72] Instead of PVA, D-glucose or cyclodextrine would result in formation of Ag/C core-shell nanocables.[73]

Table 1.2 is a summary of self-assembly micelle and capping reagent methods of surfactants reported previously in literature.

1.3.3 Vapor-Solid Phase Reaction

Contrasting with solution reaction system, some researchers developed vapor-solid phase reactions to fabricate 1D nanomaterials. The typical techniques included vapor solid reaction growth (VSRG), chemical vapor deposition (CVD) and arc discharge method.

1.3.3.1 Vapor-Solid Reaction Growth (VSRG)

Our group developed a route of vapor solid reaction growth to synthesize Cu and Ag NWs in 2003.[74, 75] CuCl encapsulated in poly(dimethylsiloxane) (PDMS) and tetrakis(trimethylsilyl) silane (TTMS, $Si(SiMe_3)_4$) as a reducing agent were sealed in a Pyrex tube under low pressure and reacted in the furnace under 473 K for 6 h. After reaction, Cu/PDMS cables were produced, as shown in Figure 1.5A and B. In the reaction process, TTMS vapor diffused
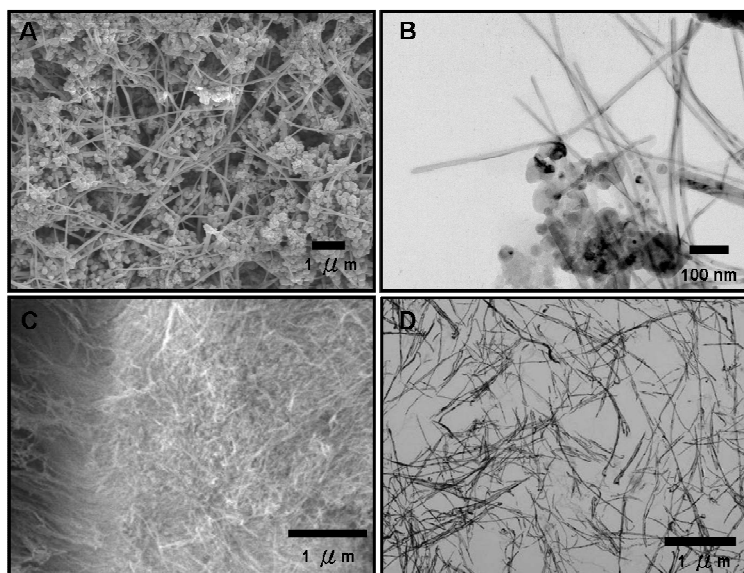
Figure 1.5 (A) SEM and (B) TEM images of Cu NWs; (C) SEM and (D) TEM images of Ag/SiO$_2$ nanocables.

across PDMS layers and reduced CuCl to form Cu atoms at the interface. These active Cu atoms aggregated and grew into NWs by PDMS directing. Subsequently, Ag/SiO$_2$ nanocables were also prepared by VSRG mechanism, as shown in Figure 1.5C and D.

1.3.3.2 Chemocal Vapor Deposition (CVD)

CVD is a traditional technique used to produce high-purity, high-performance solid materials, especially thin films in the semiconductor industry. Recently, it has become an important approach to grow 1D nanomaterials. Carbon NTs and silicon NWs grown by the vapor liquid solid (VLS) mechanism are well-known examples. In 2004, Choi et al. grew Cu NWs with the diameter of 70-100 nm on Si wafer using Cu(etac) [PEt$_3$]$_2$ (etac = ethyl 3-oxobutanoate) as a specific precursor.[76] In 2006, Wang et al. used Cu(hfac)$_2$ (hfac = hexafluroacetylacetonate) as a precursor and grew Cu nanobats with pentagonal cross section on TaN.[77] These free standing Cu NW arrays displayed electron FE properties. Besides, it is easy to construct FE panel device due to large area and selected area growth on Si. However, complicated syntheses of precursors and strict reaction condition restricted their development

Table 1.3 Vapor-solid phase method

Metal	Shape	Dimension (D diameter; L length)	Reactant	Fabricaiton technique	Reaction condition	Ref
Cu/ PDMS	Cable	D 20-80 nm; L 10 μm	$CuCl_{(s)}$/ $TTMS_{(s)}$	Vapor solid reaction growth	$PDMS_{(s)}$/sealed under low pressure / 473 K	74
Ag/ SiO$_2$	Cable	D ~25 nm; L 10 μm	$AgNO_{3(s)}$/ $TTMS_{(s)}$		sealed under low pressure / 400 K	75
Cu	Wire	D 70-100 nm	Cu (etac)$[PEt_3]_{2(l)}$		Si substrate/ 523 K	76
Cu	Bat	D_{head} 100 nm; D_{tail} 50 nm	$Cu(hfac)_{2(l)}$	CVD	TaN substrate/ 623 K	77
Cu/ C	Cable	D 30-80 nm	$anthracite_{(s)}$/ $CuO_{(s)}$	Arc-charge method	70 A/ 20 V/ $Ar_{(g)}$	78

Abbreviation

TTMS= tetrakis(trimethylsilyl)silane

PDMS= poly(dimethylsiloxane)

etac= ethyl 3-oxobutanoate

hfac= hexafluroacetylaceton

of application.

1.3.3.3 Arc Discharge Method

An electric arc is an electrical breakdown of a gas which produces an ongoing plasma discharge, resulting from a current flowing through normally nonconductive media such as air. Arc discharge process is the first and now widespread method of carbon NTs production. Wang et al. used the mixture of anthracite goal and CuO as the anode and evaporate them

under high temperature produced by DC arc discharge. Then Cu/C nanocables can be produced on the cathode.[78]

Table 1.3 is a summary of vapor-solid phase method reported in literature.

1.4 The Aim of This Thesis

In recent years, a large amount of researches with regard to Au and Ag nanomaterials has demonstrated interesting shape related physical and chemical properties. These materials have become candidates for new generation nanodevices. Their synthetic methods as mension above, nevertheless, require complex procedures, strict conditions, and unpleasantly operating equipments.

Cu and Au are highly applicable materials. Unfortunately, there are few reports regarding direct growth of 1D Cu and Au nanostructures on electrodes in the past years. We were devoted to developing a kind of method, which is able to create 1D Cu nanostructures and grow directly them on solid electrodes. It would promote more researches and development of functional devices of metal nanostructures.

In this thesis, we demonstrated that surfactant-assisted electrochemical methods, including galvanic displacement reduction and electrochemical deposition, provide a feasible approach to attain the desired goal: controllable growth of diverse Cu and Au nanostructures on solid electrodes. These products contains Cu NBs, pagoda-topped tetragonal nanopillar arrays, Au nanothorns, and nanourchins. Systematical observations by changing particularly additive concentration revealed that diffusion limited condition, surfactants, and nitric acid played a key role in controlling crystal morphologies.

Moreover, we are interested in how shape-dependent electrocatalysis and FE properties of these nanostructures are. These related studies would be presented in the following chapters.

1.5 References

1. Liu, R.; Pai, C.-S.; Martinez, E. *Solid-State Electron.* **1999,** *43*, 1003.

2. Kidwai, M.; Bansal, V.; Saxena, A.; Aerry, S.; Mozumdar, S. *Tetrahedron Lett.* **2006,** *47*, 8049.

3. Dhas, N. A.; Raj, C. P.; Gedanken A. *Chem. Mater.* **1998,** *10*, 1446.

4. Gattrell, M.; Gupta, N.; Co, A. *Journal of Electroanal.l Chem.* **2006,** *594*, 1.

5. Jiang, I.; Brisard, G. M. *Electrochim.a Acta* **2007,** *52*, 4487.

6. Xia, Y.; Yang, P.; Sun, Y.; Wu, Y.; Mayers, B.; Gates, B.; Yin, Y.; Kim, F.; Yan, H. *Adv. Mater.* **2003**, *15*, 353.

7. Chen, J.; Wiley, B. J.; Xia, Y. *J. Am. Chem. Soc.* **2007**, *23*, 4120.

8. Xia, Y.; Yang, P.; Sun, Y.; Wu, Y.; Mayers, B.; Gates, B.; Yin, Y. K., F.; Yan, H. *Adv. Mater.* **2003,** 15, 353.

9. Murphy, C. J.; Jana, N. R. *Adv. Mater.* **2002,** *14*, 80.

10. Tao, A.; Kim, F.; Hess, C.; Goldberger, J.; He, R. G.; Sun, Y. G. X., Y. N.; Yang, P. D. *Nano Lett.* **2003,** 2, 1229.

11. Yin, L. X.; Liebscher, J. *Chem. Rev.* **2007,** *107*, 133.

12. Zhao, J.; Wang, F.; Yu, J. J.; Hu, S. S. *Talanta* **2006,** *70*, 449.

13. Jena, B. K.; Raj, C. R. *Chem. Eur. J.* **2006,** *12*, 2702.

14. Wang, G.; Mantey, K.; Nayfeh, M. H.; Yau, S. T. *Appl. Phy. Lett.* **2006,** *89*, 24.

15. Hrapovic, S.; Liu, Y. L.; Male, K. B.; Luong, J. H. T. *Anal. Chem.* **2004,** *76*, 1083.

16. Ye, J. S.; Wen, Y.; Zhang, W. D.; Gan, L. M.; Xu, G. Q.; Sheu, F. S. *Electrochem. Commun.* **2004,** *6,* 66.

17. Yuan, J. H.; Wang, K.; Xia, X. H. *Adv. Funct. Mate.* **2005,** 15, (5), 803-809.

18. Zhuang, Z. J.; Su, X. D.; Yuan, H. Y.; Sun, Q.; Xiao, D.; Choi, M. M. F. *Analyst* **2008,** *133*, 126.

19. Park, S.; Chung, T. D.; Kim, H. C. *Analy. Chem.* **2003,** *75*, 3046.

20. Song, Y. Y.; Zhang, D.; Gao, W.; Xia, X. H. *Chem. Eur. J.* **2005,** *11*, 2177.

21. Bard, A. J.; Faulkner, L. R., *Electrochemical methods: Fundamentals and Applications* 2nd ed.; John Wiley & Sons Inc., New York, 2001.

22. Wang, C.; Daimon, H.; Lee, Y.; Kim, J.; Sun, S. *J. Am. Chem. Soc.* **2007,** *129*, 6974.

23. Zen, J. M.; Chung, H. H.; Kumar, A. S. *Analy. Chem.* **2002,** *74*, 1202.

24. Zen, J. M.; Hsu, C. T.; Kumar, A. S.; Lyuu, H. J.; Lin, K. Y. *Analyst* **2004,** *129*, *841*.

25. Moores, A.; Goettmann, F. *New J. Chem.* **2006,** *30*, 1121.

26. Faraday, M., *Philos. Trans.* **1857,** *147*, 145.

27. Mie, G., *Ann. Phys.* **1908,** *25*, 377.

28. Waterman, P. C. *Phys. Rev. D* **1971,** *13*, 825-39.

29. Yang, W.-H.; Schatz, G. C.; Van Duyne, R. P. *J. Chem. Phys.* **1995,** *103*, 869.

30. Duval Malinsky, M.; Kelly, K. L.; Schatz, G. C.; Van Duyne, R. P. *Analy. Chem.* **2001**, *105*, 2343.

31. Messinger, B. J.; von Raben, K. U.; Chang, R. K.; Barber, P. W. *Phy. Rev. B* **1981,** *24*, 649.

32. Jin, R.; Charles Cao, Y.; Hao, E.; Metraux, G. S.; Schatz, G. C.; Mirkin, C. A. *Nature* **2003,** *425*, 487.

33. West, J. L.; Halas, N. J. *Analy. Chem.* **2003**, *5*, 285.

34. Jeanmaire, D. L.; Vanduyne, R. P. *J. Electroanaly. Chem.***1977,** *84*, 1.

35. Zhang, X. Y.; Young, M. A.; Lyandres, O.; Van Duyne, R. P. *J. Am. Chem. Soc.* **2005,** *127*, 4484.

36. Grubisha, D. S.; Lipert, R. J.; Park, H. Y.; Driskell, J.; Porter, M. D. *Analy Chem* **2003,** *75*, 5936.

37. Shafer-Peltier, K. E.; Haynes, C. L.; Glucksberg, M. R.; Van Duyne, R. P., *J. Am. Chem. Soc.* **2003,** *125*, 588.

38. Yonzon, C. R.; Haynes, C. L.; Zhang, X. Y.; Walsh, J. T.; Van Duyne, R. P. *Analy. Chem.* **2004,** *76*, 78.

39. Bao, L. L.; Mahurin, S. M.; Haire, R. G.; Dai, S. *Ana. Chem.* **2003,** *75*, 6614.

40. Jarvis, R. M.; Brooker, A.; Goodacre, R. *Analy. Chem.* **2004,** *76*, 5198.

41. Culha, M.; Stokes, D.; Allain, L. R.; Vo-Dinh, T. *Analy. Chem.* **2003,** *75*, 6196.

42. Cao, Y. W. C.; Jin, R. C.; Mirkin, C. A. *Science* **2002,** *297*, 1536.

43. Doering, W. E.; Nie, S. M. *Anal. Chem.* **2003,** *75*, 6171.

44. Mulvaney, S. P.; Musick, M. D.; Keating, C. D.; Natan, M. J. *Langmuir* **2003,** *19*, 4784.

45. Young, M. A.; Stuart, D. A.; Lyandres, O.; Glucksberg, M. R.; Van Duyne, R. P., *Can. J. Chem.* **2004,** *82*, 1435.

46. Choi, W. B.; Chung, D. S.; Kang, J. H.; Kim, H. Y.; Jin, Y. W.; Han, I. T.; Lee, Y. H.; Jung, J. E.; Lee, N. S.; Park, G. S. *J. Chem. Phys.* **1999**, *75,* 3129.

47. Fowler, R. H.; Nordheim, L. W. *Proc. R. Soc. A* **1928,** *119*, 173.

48. Dangwal, A.; Pandey, C. S.; Muller, G.; Karim, S.; Cornelius, T. W.; Trautmann, C. *Appl. Phys. Lett.* **2008,** *92*, 063115-3.

49. Wang, J.-H.; Yang, T.-H.; Wu, W.-W.; Chen, L.-J.; Chen, C.-H.; Chu, C.-J. *Nanotechnology* **2006,** *17*, 719.

50. Kim, C.; Gu, W. H.; Briceno, M.; Robertson, I. M.; Choi, H.; Kim, K. *Adv. Mater.* **2008,** *20*, 1859.

51. Haes, A. J.; Zhao, J.; Zou, S.; Own, C. S.; Marks, L. D.; Schatz, G. C.; VanDuyne, R. P., *J. Phys. B* **2005**, *109*, 11158.

52. Choi, J.; Sauer, G.; Nielsch, K.; Wehrspohn, R. B.; Gosele, U. *Chem. Mater.* **2003,** *15*, 776.

53. Wu, Y.; Livneh, T.; Zhang, Y. X.; Cheng, G.; Wang, J.; Tang, J.; Moskovits, M.; Stucky, G. D. **2004**, *4*, 2337.

54. Gao, T.; Meng, G.; Zhang, J.; Sun, S.; Zhang, L. *Appl. Phys. A* **2002,** *74*, 403.

55. Gao, T.; Meng, G. W.; Wang, Y. W.; Sun, S. H.; Zhang, L.. *J. Phys.Cond. Matter* **2002,** *14*, 355.

56. Li, N.; Li, X. T.; Yin, X. J.; Wang, W.; Qiu, S. L. *Solid State Commun.* **2004,** 132, 841-844.

57. Walter, E. C.; Murray, B. J.; Favier, F.; Kaltenpoth, G.; Grunze, M.; Penner, R. M. *J. Phys. Chem. B* **2002,** *106*, 11407.

58. Day, T. M.; Unwin, P. R.; Wilson, N. R.; Macpherson, J. V. *J. Am. Chem. Soc.* **2005,** *127*, 10639.

59. Monson, C. F.; Woolley, A. T. *Nano Lett.* **2003,** *3*, 359.

60. Braun, E.; Eichen, Y.; Sivan, U.; Ben-Yoseph, G. *Nature* **1998**, *391*, 775.

61. Pileni, M. P.; Ninham, B. W.; Gulik-Krzywicki, T.; Tanori, J.; Lisiecki, I.; Filankembo, A. *Adv. Mater.* **1999,** *11*, 1358.

62. Wiley, B.; Sun, Y. G.; Mayers, B.; Xia, Y. *Chem. Eur. J.* **2005,** *11*, 454.

63. Sun, Y.; Xia, Y. **2002,** *298*, 2176.

64. Sun, Y. G.; Mayers, B.; Herricks, T.; Xia, Y. N. **2003,** *3*, 955.

65. Huang, T. K.; Cheng, T. H.; Yen, M. Y.; Hsiao, W. H.; Wang, L. S.; Chen, F. R.; Kai, J. J.; Lee, C. Y.; Chiu, H. T. *Langmuir* **2007,** *23*, 5722.

66. Liu, Z.; Yang, Y.; Liang, J.; Hu, Z.; Li, S.; Peng, S.; Qian, Y. *J. Phys. Chem. B* **2003,** *107*, 12658.

67. Chang, Y.; Lye, M. L.; Zeng, H. C. *Langmuir* **2005,** *21*, 3746.

68. Shi, Y.; Li, H.; Chen, L.; Huang, X. *Sci. and Technol. Adv. Mater.* **2005,** *6*, 761.

69. Wang, Z.; Liu, J.; Chen, X.; Wan, J.; Qian, Y. *Chem. Eur. J.* **2005,** *11*, 160.

70. Xu, J.; Hu, J.; Peng, C.; Liu, H.; Hu, Y. *J. Colloid Interface Sci.* **2006,** *298*, 689.

71. Gong, J.; Luo, L.; Yu, S. H.; Qian, H.; Fei, L. *J. Mater. Chem.* **2006,** *16*, 101.

72. Luo, L. B.; Yu, S. H.; Qian, H. S.; Zhou, T. *J. Am. Chem. Soc.* **2005,** *127*, 2822.

73. Yu, S. H.; Cui, X. J.; Li, L. L.; Li, K.; Yu, B.; Antonietti, M.; Coelfen, H. *Adv. Mater.* **2004,** *16*, 1636.

74. Yen, M. Y.; Chiu, C. W.; Hsia, C. H.; Chen, F. R.; Kai, J. J.; Lee, C. Y.; Chiu, H. T. *Phys. Lett.* **1999,** *75*, 627.

75. Hsia, C. H.; Yen, M. Y.; Lin, C. C.; Chiu, H. T.; Lee, C. Y. *J. Am. Chem. Soc.* **2003,** *125*, 9940.

76. Choi, H.; Park, S. H. *J. Am. Chem. Soc.* **2004**, *126*, 6248.

77. Wang, J. H.; Yang, T. H.; Wu, W. W.; Chen, L. J.; Chen, C. H.; Chu, C. J. *Nanotechnology* **2006**, *17*, 719.

78. Wang, Z.; Zhao, Z.; Qiu, J. **2006**, *44*, 1845.

Chapter 2

Growth of Cu Nanobelts by Surfactant-Assisted Galvanic Reductions

---

2.1 Introduction

Nanobelts are interesting one dimensional materials under intensive investigation.[1-15] There are many reports regarding the syntheses and applications of nanobelts of semiconductors and main group elements.[1-7] On the other hand, transition metal nanobelts are much less reported. The only known example is the preparation of Ni nanobelt by a hydrothermal method and Au nanobelt by a sonochemical method.[8,9] Here, we report a surfactant assisted synthesis of single crystalline cubic phase 3C Cu nanobelt via galvanic reductions of $CuCl_{2(aq)}$ solutions in the presence of CTAC (cetyltrimethylammonium chloride) by $Al_{(s)}$. To our knowledge, this is the first example of Cu nanobelt reported to this date. We expect the metallic nanobelts, with metallic conductivity and increased surface area, may find future applications as electrodes in sensing devices,[16,17] as contacts for molecular electronic circuits,[18] in surface-enhanced Raman scattering (SERS) spectroscopy,[19,20] and in metal-polymer composites for electromagnetic interference (EMI) shielding layers.[21]

2.2 Experimental

2.2.1 Preparation of Cu Nanobelts

A summary of growth conditions is listed in Table 2.1. Growth of Cu NBs by galvanic reduction of $CuCl_{2(aq)}$ by $Al_{(s)}$ in the presence of CTAC and HNO_3 (Belt-6) is described below as a typical example.

$CuCl_2$ (Strem, 0.034 g, 0.25 mmol) was added to a stirring aqueous solution (50 mL) of

Table 2.1 Summary of growth conditions of Cu nanostructures.

Sample	CuCl$_2$ (mM)	CTAC (mM)	HNO$_3$ (mM)	Temperature (^{o}C)	Time (h)
Wire-1	5	0.45	-	17	3
Wire-2	5	1.78	-	17	3
Wire-3	5	3.56	-	17	3
Wire-4	5	1.78	-	17	3.5
Belt-1	5	1.78	0.5	17	20
Belt-2	5	1.78	5	17	20
Belt-3	5	1.78	30	17	20

CTAC (Taiwan Surfactant, 1.78 x 10^{-3} M) and HNO$_3$ (SHOWA, 5 x 10^{-3} M) in a glass vial. Immediately, the mixture turned light blue. The mixture was then placed in a water bath controlled at 290 K. An Al TEM grid (Agar, 200 mesh), cleaned in H$_3$PO$_{4(aq)}$ (Riedel-de Haen, 5 % w.t., 3 mL) for 2 m and rinsed by deionized water, was immersed into this mixture. The reaction was controlled at 290 K without stirring. The Al surface turned dark red gradually. After 24 h, the Al grid was removed and rinsed by deionized water.

2.2.2 Characterization

The air-dried samples were investigated by SEM (Hitachi S-4000 at 25 kV and JEOL JSM-6330F at 15 kV), EDS (Oxford Link Pentafet) and TEM (JEOL JEM-2010F at 200 kV and JEOL JEM-4000EX) instruments. The colloid was analyzed by an X-ray diffractometer (XRD, Bruker AXS D8 Advance) and a particle analyzer (Honeywell Microtrac UPA 150).

2.3 Results

2.3.1 SEM and EDS characterization
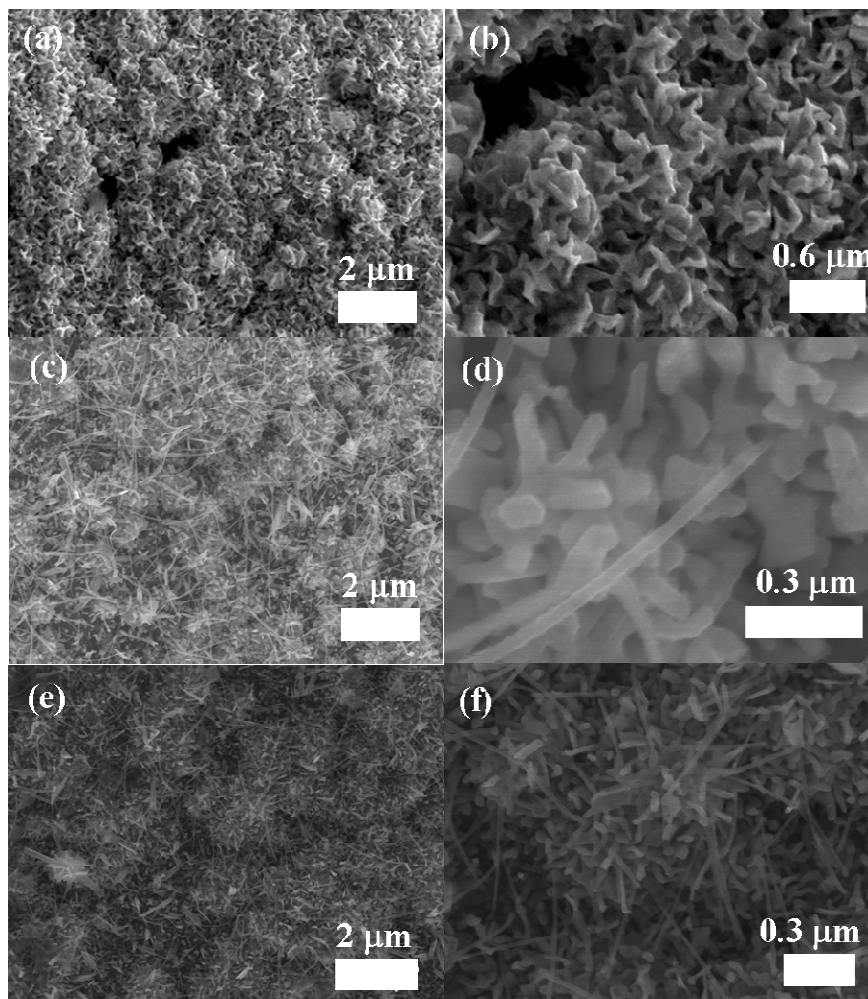
Figure 2.1 Low and high magnification SEM images of Cu nanostructures growing in solution of different CTAC concentration. (a)-(b) 0.45 mM (Wire-1), (c)-(d) 0.178 mM (Wire-2), and (e)-(f) 3.56 mM (Wire-3).

$CuCl_2$ in an aqueous solution was reduced by an Al transmission electron microscopic (TEM) grid (Agar, 200 mesh) at 290 K. As the reaction progressed, the Al surface turned dark red gradually.

Figure 2.1 shows SEM images of Sample Wire-1, Wire-2, Wire-3 in an aqueous solution of CTAC concentration at 0.45 mM, 1.8 mM, and 3.6 mM, respectively. Figure 2.1a and b show that Wire-1 has a particle layer formed on the Al grid in 0.45 mM $CTAC_{(aq)}$ solution.
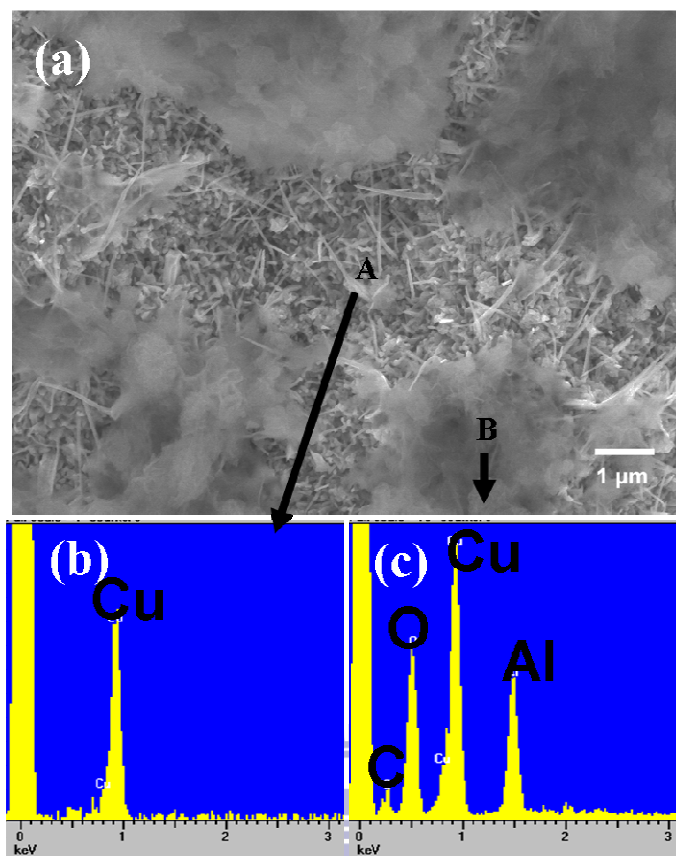
Figure 2.2 (a) SEM image of the products growing at 3.5 h (Wire-4); (b) EDS of the area marked by A in (a); (c) EDS of the area marked by B in (a).

Figure 2.1c and d show that Wire-2 grows a little of NWs with a length of about 2 μm from a particle layers as CTAC concentration increases to 1.8 mM. Instead, Wire-3 prepared in higher CTAC concentration, 0.36 mM grew less NWs, as shown in Figure 2.1e and f. It indicates that appropriate CTAC concentration assisted formation of NWs.

When elongating growth time, there are many amorphous clusters depositing on Wire-4, as shown in Figure 2.2 (a). EDS analysis suggests that NWs indicated by A consist of Cu and amorphous clusters marked by B are composed of aluminum oxide. Obviously, deposition of aluminum oxide disturbs the growth of Cu NWs.

In order to avoid interference of aluminum oxide, we choose to add nitric acid to increase dissolution of aluminum oxide in solution. Sample Belt-1, Belt-2, and Belt-3 were prepared
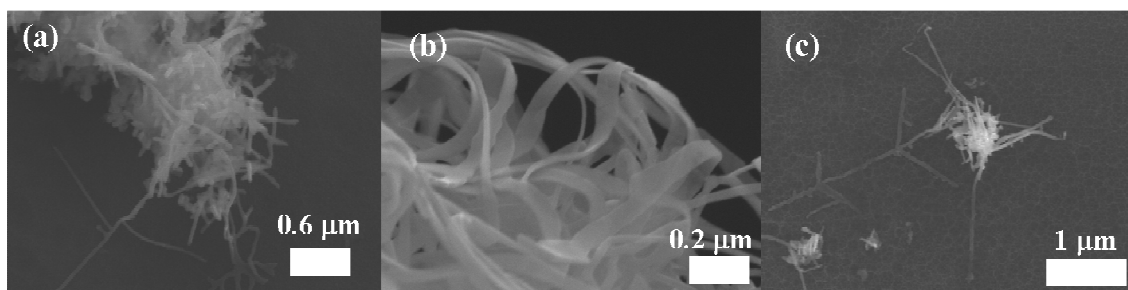
Figure 2.3 SEM images of Cu nanostructures growing in the presence of different HNO_3 concentration. (a) 0.5 mM (Belt-1); (b) 5.0 mM (Belt-2); and (c) 30.0 mM (Blet-3).

in 0.5, 5, and 30 mM HNO_3 aqueous solution, respectively. Figure 2.3 shows amorphous aluminum oxide disappears and 1D nanostructures appear on Al grid. Especially, Figure 2.3(b) shows a ribbon-like nanostructure grows densly across the grid. Generally, the nanobelt has a width of 30 - 150 nm, a thickness less than 15 nm and a length up to 10 μm. Thus, the width-to-thickness and the length-to-width ratios are as high as 10 and 300, respectively. Normally, these characters are maintained across an entire nanobelt.

2.3.2 XRD analysis

XRD pattern of Belt-3 are shown in Figure 2.4. It shows combination of two-set patterns. One has peaks at 2θ = 38.4°, 44.8°, 65.1°, and 78.2°, which are assigned to Al (111), (200), (220) and (311) reflections, respectively (JCPDF 04-0787). Al reflection is from TEM Al grid. The other has peaks at 2θ = 43.4°, 50.6°, 74.2°, which are assigned to Cu (111), (200), and (220) reflections, respectively.[22] Calculated lattice constant a, 0.361 nm, is close to the reported value of Cu.[22] This XRD study suggested that 3C Cu was grown on the Al.

2.3.3 TEM characterization

Low magnification TEM image in Figure 2.5A display an interlacing net composed of Cu NBs. Figure 2.5B shows characteristic ripple-like images from the strains of belt bending.
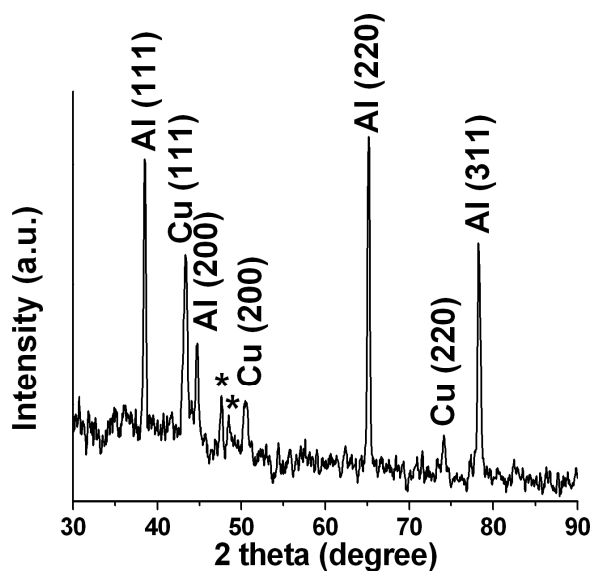
Figure 2.4. XRD pattern of Cu NBs grown on an Al grid (* = unknown)
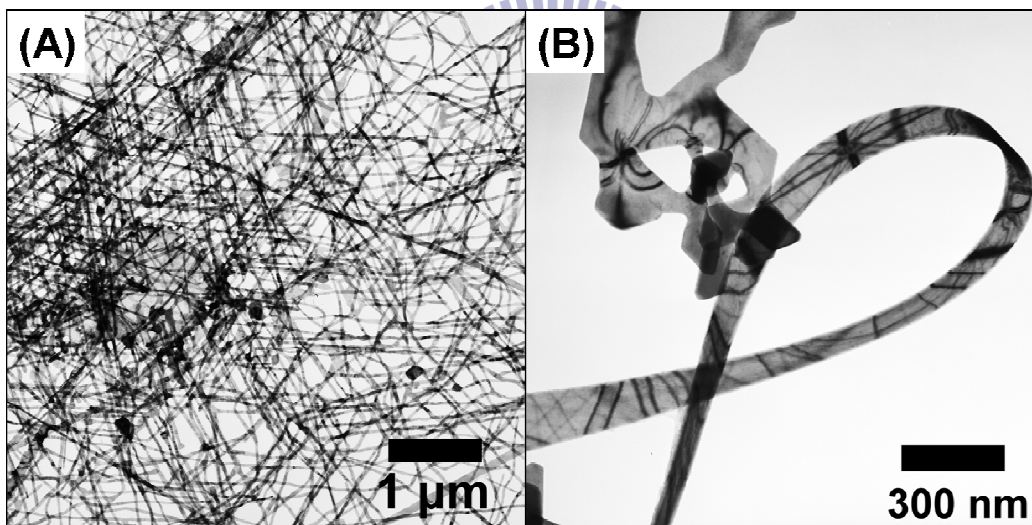
Figure 2.5. (A) Low and (B) high magnification TEM images of Cu NBs.

This feature was frequently observed in TEM studies for thin samples.[1-15]

In Figure 2.6, a set of excellent quality TEM images of a selected NB, examined from a properly adjusted angle, are shown. In Figure 2.6A, ripple-like contrasts arise from belting are observed again.[1-15] The SAED in Figure 2.6B displays a spot pattern from the rectangular region marked by a dotted arrow in Figure 2.6A. This can be indexed to be
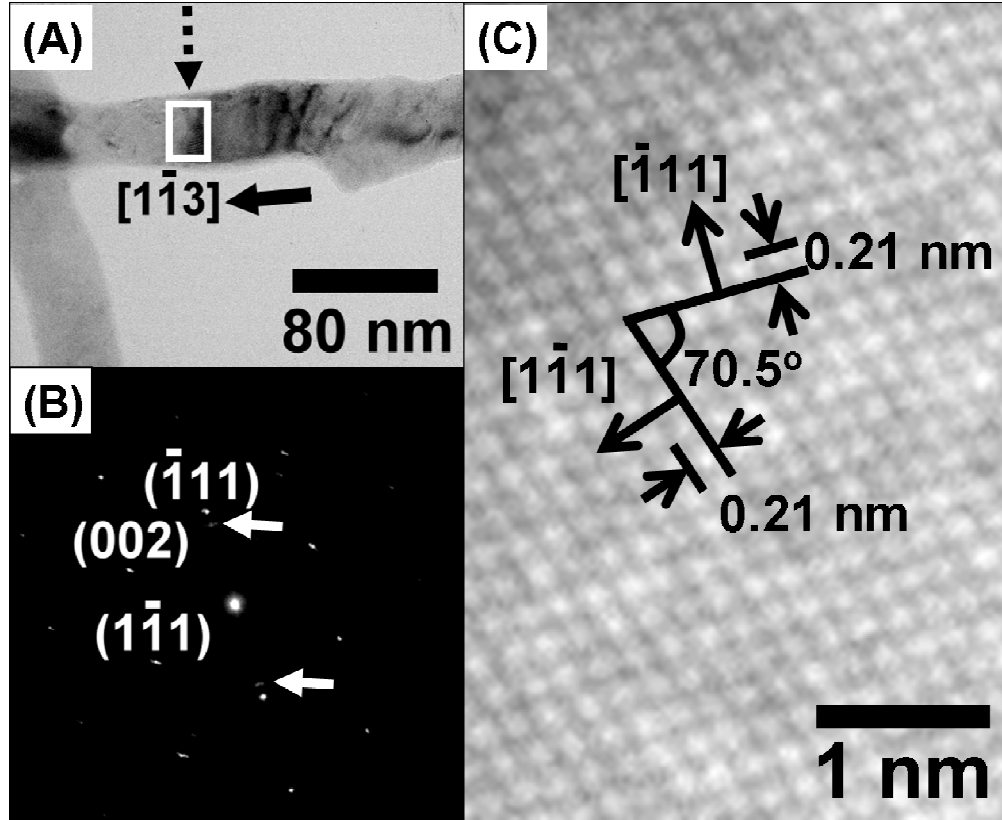
Figure 2.6. (A) TEM image of Cu nanobelts, (B) [1,1,0] zone SAED, and (C) HRTEM image of the marked rectangular region pointed by the dotted arrow in (A).

[1,1,0] zone axis of Cu, with an estimated lattice parameter of 0.36 nm. From the pattern, the apparent growth direction of the NB is determined to be along [1,-1,3] direction. From two tiny dim spots indicated by the arrows in Figure 2.6B, a d-spacing of 0.25 nm is estimated. This indicates the presence of a minute quantity of Cu_2O, which has a {1,1,1} spacing distance close to the observed value.[23] The origin is proposed to be some oxidation on the nanobelt surface. Figure 2.6C presents an HRTEM image from the marked region in Figure 2.6A. The directions of planes {1,-1,1} and {-1,1,1} are identified from the fringes. The dihedral angle of 70.5° is equal to the theoretical value of an f.c.c. structure. The {1,1,1} d spacing is measured to be 0.21 nm, close to the literature value of Cu, 0.208 nm.[22]

$M_{2}^{n+}{}_{(aq)}$

$M_{2}^{n+}{}_{(aq)}$ $M_{2}^{n+}{}_{(aq)}$

$M_{2(s)}$

$M_{1}^{m+}{}_{(aq)}$

$M_{1}^{m+}{}_{(aq)}$ $M_{1}^{m+}{}_{(aq)}$

e^{-}

$M_{1(s)}$ e^{-} e^{-}

$= CH_3(CH_2)_{15}N(CH_3)_3^+Cl^- (CTAC)$

Case 1: M_1 = Al, m = 3; M_2 = Cu, n = 2
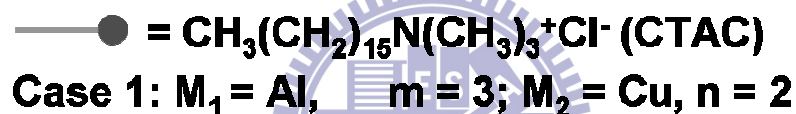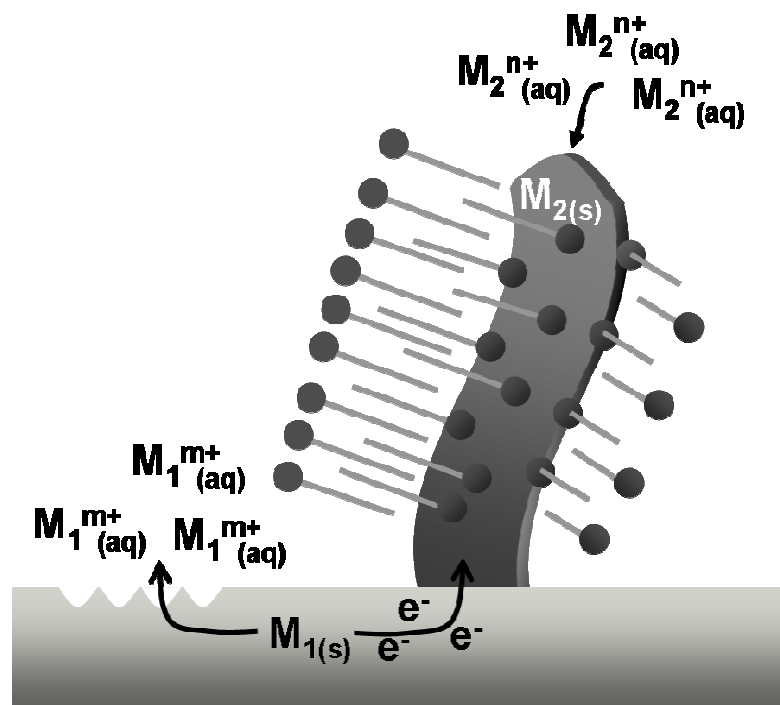
Scheme 2.1. Proposed growth mechanism of Cu nanobelt.

2.3.4 Proposed Growth Mechanism

We discovered that adding HNO_3 to the reaction mixture is important for the process. Without it, a large amount of aluminum oxide deposit blocked the Al surface and interrupted the Cu growth. The acidic environment probably assists the aluminum oxide dissolution so that active Al metal surface can be exposed. The addition of CATC is also essential to the NB formation. Without the surfactant, only dendridic structures were produced. The physical forms of Al metal did not affect the Cu NB growth much. We tried several types of Al, including powders, foils and plates. They all showed similar results.

The preparation of both Cu NB is dependent on the presence of CTAC. Without it, the uncontrolled growths produce dendridic structures.[24-27] A generalized CTAC assisted NB growth is presented in Scheme 1 to describe the overall growth process. Galvanic reduction

33

of $Cu^{2+}_{(aq)}$ by more active $Al_{(s)}$ to form Cu NBs is described. The $Cu^{2+}_{(aq)}$ ions are reduced, then nucleate into Cu metal on the Al surface. The reaction is spontaneous due to a positive redox potential E^o = 2.00 V, for the reaction 3 $Cu^{2+}_{(aq)}$ + 2 $Al_{(s)}$ → 3 $Cu_{(s)}$ + 2 $Al^{3+}_{(aq)}$.[28] CTAC molecules probably adsorb selectively on two crystallographically opposite facets of a Cu seed to form a bilayer interface structure.[29, 30] Through the ionic ends of the surfactant molecules, one side of the CTAC bilayer binds to the Cu surface while the other side interfaces with the aqueous medium. Between two ionic sides, the aliphatic chains form an inner nonpolar sheet. This specific arrangement restricts the deposition of Cu atoms on the CTAC passivated facets. Consequently, the Cu crystal grows within the CTAC bilayer constructed soft template and develops into a NB.

2.4 Conclusion

In summary, we have demonstrated the first time that Cu NB can be grown via simple galvanic reductions of the corresponding metal ions by active metals in the presence of CTAC in aqueous solutions. Both CTAC and HNO_3 molecules are essential ingredients to shape the highly symmetric fcc Cu crystals into the belt morphology.

2.5 References

1. Wang, Z. L., *Adv. Mater.* **2003**, *15*, 432.

2. Pan, Z. W.; Dai, Z. R.; Wang, Z. L. *Science* **2001**, *291*, 1947.

3. Shi, W. S.; Peng, H. Y.; Wang, N.; Xu, C. P.; Li, L.; Lee, C. S.; Lee, S. T. *J. Am. Chem. Soc.* **2001**, *123*, 11095.

4. Ma, Y.; Qi, L.; Shen, W.; Ma, J. *Langmuir* **2005**, *21*, 6161.

5. Cao, X. B.; Xia, Y.; Zhang, S. Y.; Li, F. Q. *Adv. Mater.* **2004**, *16*, 649.

6. Mo, M.; Zeng, J.; Lin, X.; Yu, W.; Zhang, S.; Qian, Y. *Adv. Mater.* **2002**, *14*, 1658.

7. Zhang, M.; Wang, Z.; Xi, G.; Ma,D.; Zhang, R.; Qian, Y. *J. Cryst. Growth* **2004**, *268*, 215.

8. Liu, Z.; Li, S.; Yang, Y.; Peng, S.; Hu, Z.; Qian, Y *Adv. Mater.* **2003**, *15*, 1946.

9. Zhang, J. L.; Du, J. M.; Han, B. X.; Liu, Z. M.; Jiang, T.; Zhang, Z. F. *Angew. Chem. Int. Ed.* **2006**, *45*, 1116.

10. Wang, Y.; Zhang, L.; Meng, G.; Liang, C.; Wang, G.; Sun, S. *Chem. Commmun.* **2001**, *24* ,2632.

11. Xie, Z.; Wang, Z.; Ke, Y.; Zha, Z.; Jiang, C. *Chem. Lett.* **2003**, *32*, 686.

12. Sun, Y.; Mayers, B.; Xia, Y. *Nano Lett.* **2003**, *3*, 675.

13. Law, M.; Sirbuly, D.; Johnson, J.; Goldberger, J.; Saykally, R.; Yang, P. *Science* **2004**, **305**, 1269.

14. Yan, H.; Justin, J.; Law, M.; Saykally, R.; Yang, P. *Adv. Mater.* **2003**, *15*, 1907.

15. Law, M.; Kind, H.; Kim, F.; Messer, B.; Yang, P. *Angew. Chem. Int. Ed*. **2002**, *41*, 2405.

16. Zen, J. M.; Chung, H. H.; Kumar, A. S. *Anal. Chem.* **2002**, *74*, 1202.

17. Zen, J. M.; Chung, H. H.; Kumar, A. S. *Analayst* **2000**, *125*, 1633.

18. Tour, J. M *Molecular Electronics: Commercial Insights, Chemistry, Devices, Architecture and Programming*, World Scientific, Singapore, **2003**, p. 229-250.

19. Kneipp, K.; Wang, Y.; Kneipp, H.; Perelman, L. T.; Itzkan, I.; Dasari, R.; Feld, M. S. *Phys. Rev. Lett.* **199**7, *78*, 1667.

20. Nie, S. M.; Emory, S. R. *Science* **1997**, *275*, 1102.

21. Bagwell, R. M.; McManaman, J. M.; Wetherhold, R. C. *Compos. Sci. Tech.* **2006**, *66*, 522.

22. Joint Committee for Powder Diffraction (JCPDS) File No. 04-0836, International Center for Diffraction Data (ICDD), **1982**.

23. JCPDS File No. 05-0667, ICDD, **1953**.

24. Ben-Jacob, E.; Garik, P. *Nature* **1990**, *343*, 523.

25. Shin, H. C.; Dong, J.; Liu, M. *Adv. Mater.* **2003**, *15*, 1610.

26. Wang, S.; Xin, H. *J. Phys. Chem. B* **2000**, *104*, 5681.

27. Ma, Y.; Che, C. M.; Chao, H. Y.; Zhou, X.; Chan, W. H.; Shen, J. *Adv. Mater.* **1999**, *11*, 850.

28. Bard, A. J.; Faulkner, L. R. *Electrochemical Methods: Fundamentals and Applications*, John Wiley & Sons, New York, **1980**.

29. Gao, J.; Bender, C. M.; Murphy, C. J. *Langmuir* **2003**, *19*, 9065.

30. Nikoobakht, B.; El-Sayed, M. A. *Langmuir* **2001**, *17*, 6368.

Chapter 3

Electrochemical Growth of Copper Nanobelt Electrode for Glucose Sensing

---

3.1 Introduction

More than 180 million people worldwide are suffering from diabetes.[1] Commercial pocket-sized blood sugar sensors based on glucose oxidase electrodes have benefited patients for conveniently monitoring their blood sugar concentration variations at any time.[2-7] Recently, there are more and more developments in nanostructured non-enzymatic sensors because they can overcome the disadvantages of enzymatic designs, including intrinsic instability, complicated immobilization processes, and oxygen concentration dependent environment. The nanostructured electrodes with high electroactive surfaces can enhance current response and increase sensing selectivity of glucose. Sensors constructed from nanostructured Pt, Au, Si, carbon nanotube (CNT), CNT/metal composite and CuO electrodes are known examples.[8-16] However, the reported preparations are complicated and sometimes provide irreproducible results. To overcome the deficiencies mentioned above, in this report, we discuss our exploration of a simple electrochemical deposition of Cu nanobelts (NBs) on carbon as electrodes for glucose sensing. Metal nanobelts are relatively new.[17-24] As mention early, calculations show that NBs possess surface areas higher than nanoparticles (NPs) and nanowires (NWs) with comparable dimensions over 40 nm.

3.2 Experimenal

3.2.1 Preparation of Cu NB electrodes

CuCl$_2$ (0.034 g, 0.25 mmol) was added to a stirring aqueous solution (100 mL) of CTAC

(0.9 mM) and HNO_3 (2.5 mM) in a glass vial. Immediately, the mixture turned light blue. After a portion of the solution (10 mL) was transferred to another glass vial, it was placed in a water bath controlled at 290 K. The Cu NB was grown on the cathode in a two-electrode electrochemical cell composed of a DC power supply and two carbon electrodes. The cathode was a carbon screen printed electrode (SPE), purchased from Zensor R&D with a geometric area of 0.018 cm^2. The anode was fabricated by painting carbon paste uniformly on transparent projection slides followed by drying them on a hotplate at 353 K for 3 h under air. They were cleaned with deionized water before use. After the cathode and the anode were immersed in the reaction mixture for 3 min, a fixed DC voltage of 2.0 V was supplied across the electrodes. At 290 K without stirring, the cathode surface turned into a copper-like color gradually. After 24 h, a total charge of ca 0.5 C was supplied. The cathode was removed and rinsed with deionized water. To avoid oxidation, the as-prepared Cu NB electrodes were stored in a N_2 filled glove box.

3.2.2 Preparation of Cu NP and foil electrodes

For comparison of electrochemical properties, Cu NP and Cu foil electrodes were also fabricated. Cu NPs were electrochemically grown on SPE using the same reduction charge of 0.5 C in an aqueous mixture of 200 ppm $Cu(NO_3)_2$ and 0.1 M HNO_3. Cu foils (Aldrich), with exposed geometric area of 0.018 cm^2, were prepared by covering their surfaces with properly sized Scotch tapes (3M).

3.2.3 Characterization

The electrodes were characterized by the following instruments: SEM (JEOL JSM-6330F at 15 kV), EDS (Oxford Link Pentafet), FETEM (JEOL JEM-2010F at 200 kV and JEOL JEM-4000EX), and X-ray diffraction (XRD) (Bruker AXS D8 Advance). CV and chronoamperometric experiments were carried out using a CHI 802 electrochemical
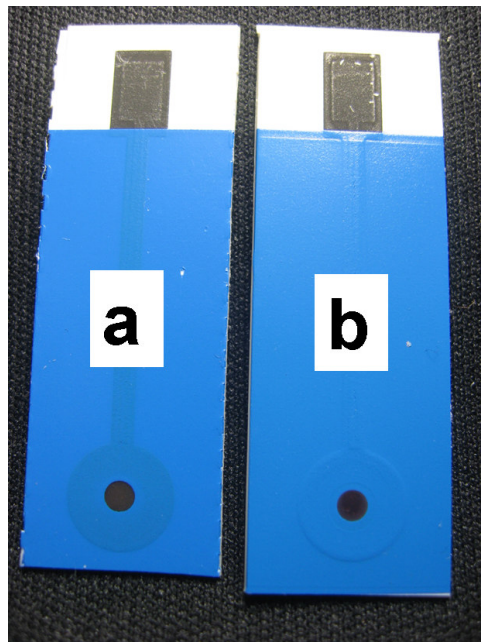
Figure 3.1. Photographs of (a) Cu NP and (b) Cu NB electrodes.

workstation (CH Instruments, Austin, TX, USA). Amperometric curve of the electrodes was recorded at 0.6 V in a stirring 50 mM NaOH solution in air.

3.3 Results

As mention in Chapter 2, we demonstrated the growth of Cu NBs on $Al_{(s)}$ surface from galvanic reduction of $Cu^{2+}_{(aq)}$ by $Al_{(s)}$ in the presence of cetyltrimethylammonium chloride (CTAC) and $HNO_{3(aq)}$.[24] In this study, we modified the process. Cu NBs were deposited electrochemically from an aqueous solution of $CuCl_2$, CTAC and HNO_3 on printed carbon electrodes at 290 K. Instead of $Al_{(s)}$, a constant reduction potential of 2.0 V was provided by a DC power supply.

3.3.1 SEM Characterization and Belt Width Histogram

Figure 3.1 shows photographs of as prepared Cu NB and NP electrodes. The product is electro-deposited on the dark circle carbon electrode with a confined geometry area of 0.018
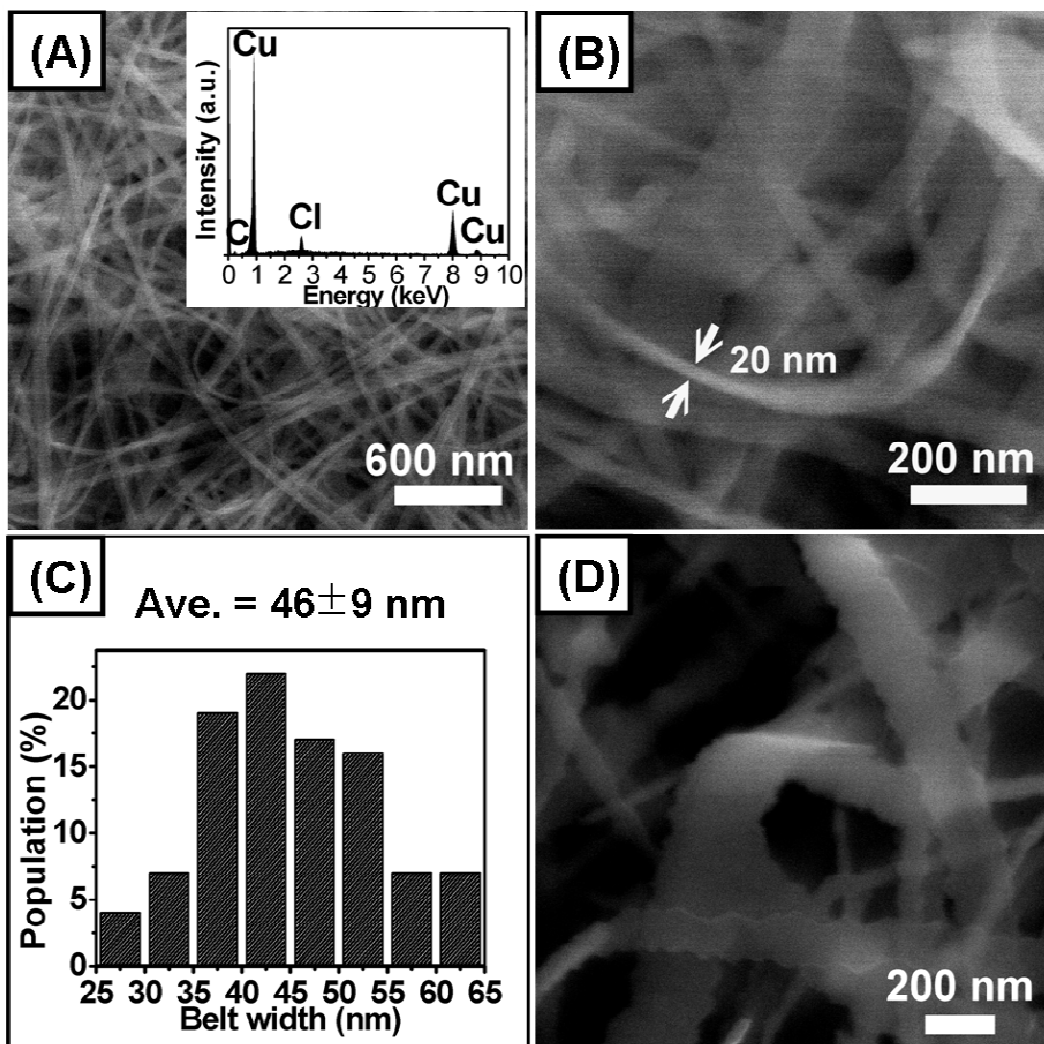
Figure 3.2. (A) Typical SEM image and EDS (inset) of Cu NBs grown on carbon electrode, (B) enlarged view showing bending and thickness of NBs, (C) belt width distribution histogram of NBs in (A), (D) wide NBs grown at a different concentration.

cm^2. Figure 3.2 shows the data from scanning electron microscopic (SEM) characterizations of the as-prepared product on electrode. As displayed in Figure 3.2A, 1-D nanostructures, several tens of μm in length, grow densely to cover the entire carbon electrode surface. The energy dispersive spectrum (EDS, inset) confirms that the product is composed of Cu mainly. Traces of C and Cl from CTAC capping the NB surface are observed also.[24] Figure 3.2B shows clearly a bending belt with a thickness of 20 nm. In Figure 3.2C, a width

distribution histogram of 100 NBs in Figure 3.2A is shown. This provides an average width of 46 nm and a main distribution range of 35 - 55 nm. The belt width can be adjusted by varying the reaction mixture concentration and the applied potential. For example, when all ingredients in the mixture was doubled, the NBs display increased width (average: 185 nm, main distribution: 120 - 240 nm) and zigzag edges, as shown in Figure 3.2D and 3.3.
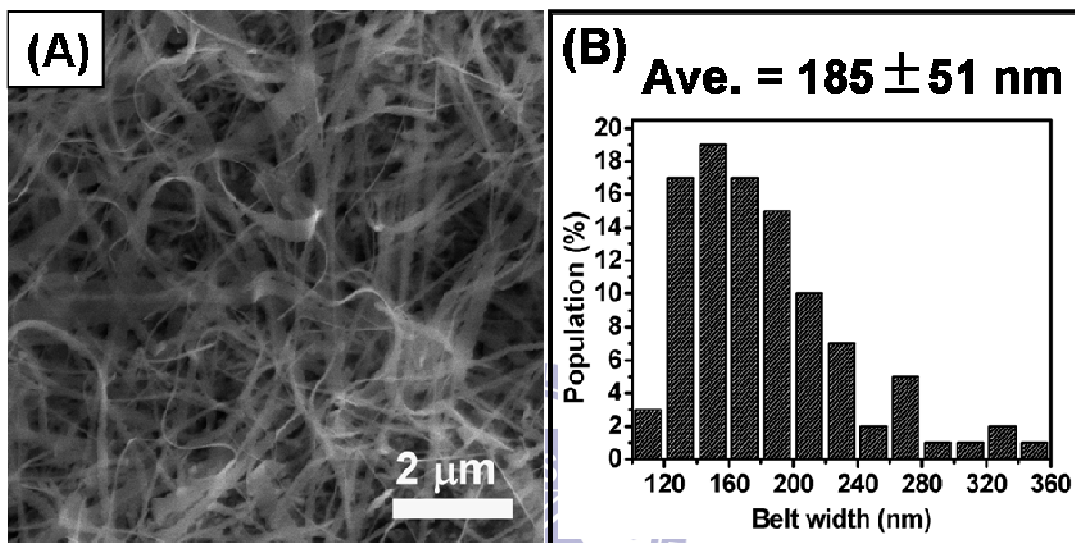
Figure 3.3. (A) SEM images of Cu NBs prepared in solutions of 5.0 mM $CuCl_2$ / 1.8 mM CTAC / 5.0 mM HNO_3; (B) belt width distribution histogram of NBs in (A).

Figure 3.4 shows that SEM image of Cu NPs grown on electrode. The diameter is uneven and in the range of 50-200 nm.

3.3.2 XRD Analysis

XRD pattern of NBs grown on electrode is shown in Figure 3.5. The peaks at $2\theta = 43.0^o$, 50.2^o, and 74.0^o are assigned to Cu (111), (200), and (220) reflections, respectively (JCPDF 89-2838). Lattice constant a is estimated to be 0.362 nm, is consistent with the reported value of Cu (JCPDF 89-2838). The other peaks at $2\theta = 53.1^o$, 54.6^o, 55.8, and 68.0^o are contributed to carbon electrode. XRD patterns also confirmed that the NBs had an fcc

structure.
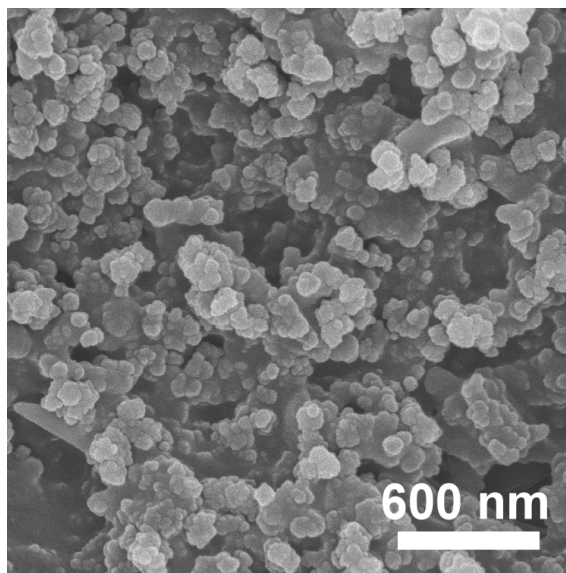
Figure 3.4. SEM image of Cu NPs grown on carbon electrode.
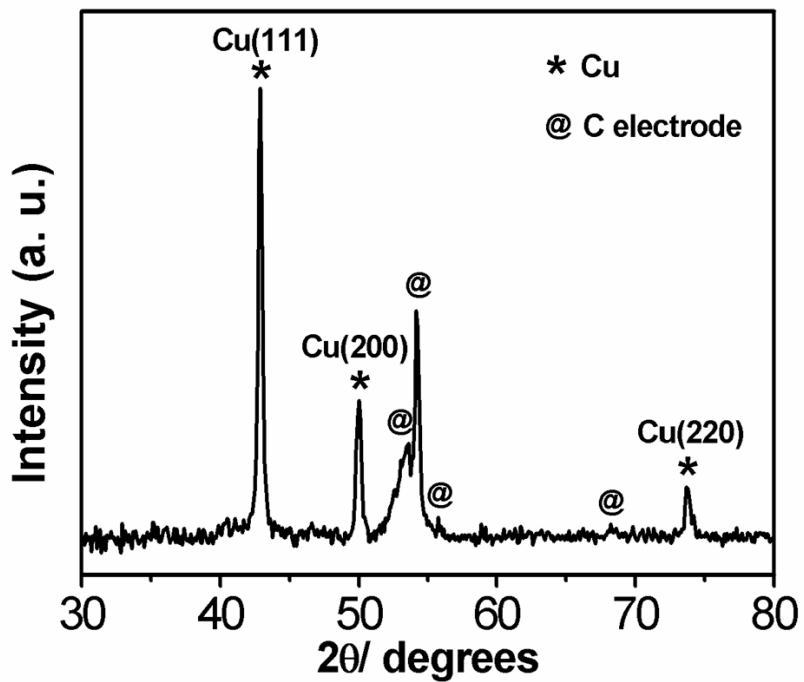
Figure 3.5. XRD pattern of Cu NBs grown on carbon electrode.
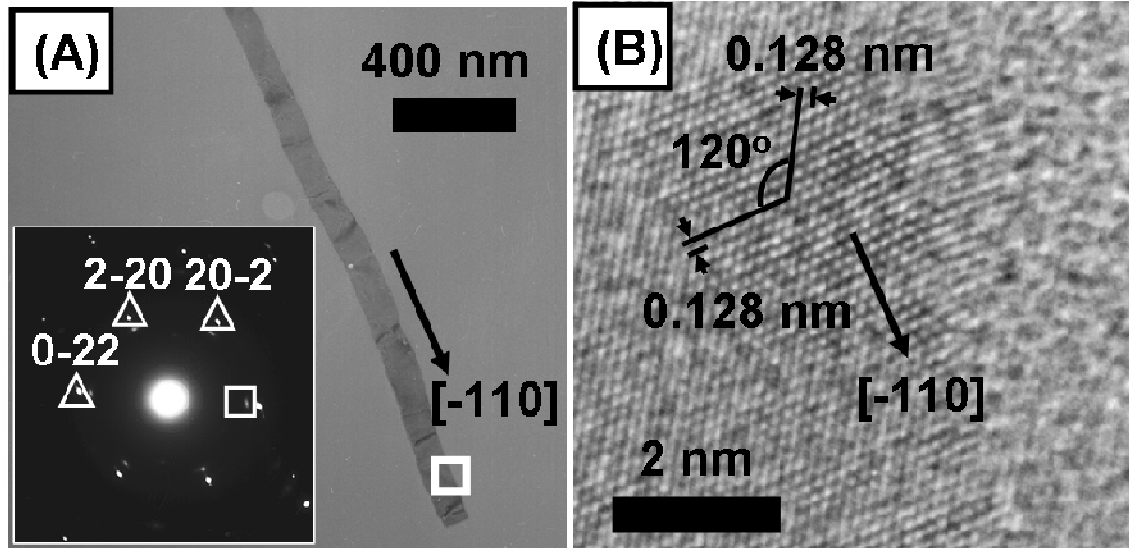
Figure 3.6. (A) TEM image and SAED pattern (inset) from the white square of an individual Cu NB, and (B) HRTEM image from the white square in (A).

3.3.3 TEM Characterization

In Figure 3.6A, the TEM image of a single NB lying flatly is shown. Dark lines from internal stresses, typical for NB materials, are clearly observed.[17-32] The selected area electron diffraction (SAED, inset) displays a set of dots with a hexagonal symmetry, exemplified by three spots marked with triangles. This indicates that the NB was single-crystalline. From the pattern, the crystallographic zone axis can be indexed to be Cu [111]. The brightest set of spots is assigned to Cu {220} reflections (JCPDF 89-2838) with a d-spacing of 0.128 nm. It also indicates that the NB's basal plane was {111}. Growth direction of the NB is determined to be along [-110] direction as concluded from the SAED pattern. Figure 3.6B presents an HRTEM image from the marked region in Figure 3.6A. Two {220} lattice planes are identified on the basis of their dihedral angle of 120°. This is consistent with the theoretical value of an fcc structure. The d-spacing is measured to be 0.128 nm, close to the literature value of Cu, 0.1278 nm (JCPDF 89-2838). These HRTEM characterizations agree with the SAED result. The estimated lattice parameter *a*, 0.36 nm, is
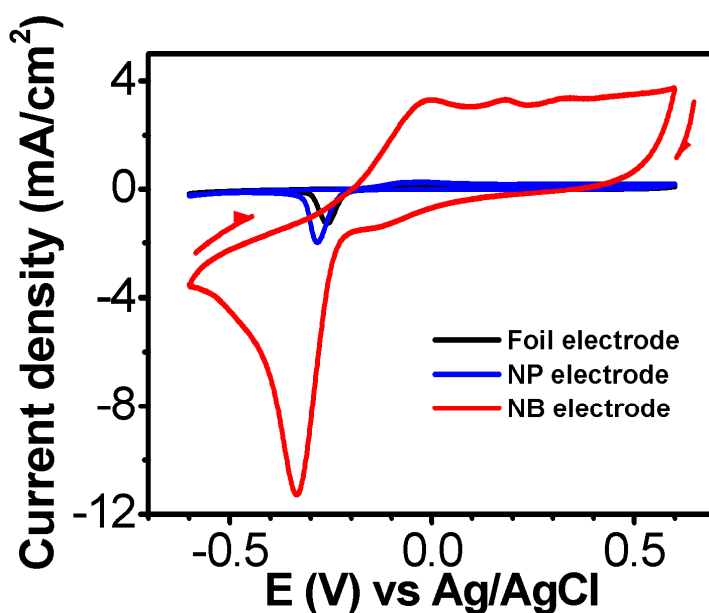
Figure 3.7. CVs of Cu foil (black), NP (blue) and NB (red) electrodes in pH 7.4 PBS at scan rate 50 mV/s.
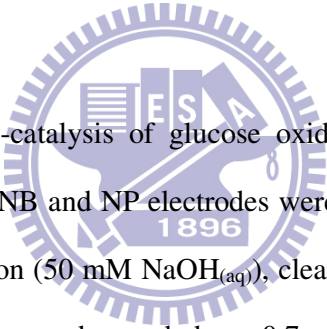
consistent with the reported value of Cu, 0.362 nm (JCPDF 89-2838). In the SAED in Figure 3.6A, in addition to the pattern of Cu, there is another set of dimmer hexagonal spots, exemplified by the one marked with a white square. This suggests the presence of another cubic phase material with a d-spacing of 0.25 nm. This is close to the {111} spacing value of Cu_2O, 0.246 nm (JCPDF 78-2076). Origin of the minute quantity of Cu_2O is proposed to be from oxidation of the NB surface under an ambient condition.

3.3.4 Cyclic Voltammetric Characterization

In order to study the possible application of our NBs on printed carbon electrodes, we fabricated two other types of Cu electrodes, constructed from a Cu foil and Cu NPs on printed carbon, for comparison. All these had an identical geometric area of 0.018 cm^2. Both of the NB and the NP electrodes were electrochemically grown using the same reduction charge of 0.5 C.[33] Figure 3.7 shows the cyclic voltammetric (CV, scan rate = 50 mV/s)

behaviors of these electrodes in a phosphate buffer solution (PBS, pH = 7.4). For the NB electrode, it shows significantly higher reduction/oxidation responses than the other two do. This indicates that the NB electrode has a relatively large electrochemical surface area.[33] The oxidation peaks at -0.02, 0.18 and 0.32 V are referred to the conversion of Cu(0) to Cu(I), Cu(I) to Cu(II) and Cu(II) to Cu(III).[15] In the reduction cycle, the peak at -0.33 V and the shoulder at -0.46 V correspond to the translations of Cu(II) to Cu(I) and Cu(I) to Cu(0), respectively.[33] The other weak wave at -0.14 V is assigned to the conversion of Cu(III) to Cu(II). It is surprising that the reductive peak intensity of the NP electrode is only one seventh of that of the NB electrode. This suggests that the aggregated NPs could not expose their surfaces as efficiently as the NBs.

3.3.5 Glucose Sensing

In order to compare electro-catalysis of glucose oxidation by the nanostructured Cu electrodes, CV studies of both NB and NP electrodes were performed. As shown in Figure 3.8A, in a blank alkaline solution (50 mM NaOH$_{(aq)}$), clear current increases corresponding to a Cu(II)/Cu(III) redox couple are observed above 0.7 and 0.75 V for the NB and the NP electrodes, respectively.[14] For both electrodes in 0.1 M glucose mixed with 50 mM NaOH$_{(aq)}$, additional waves, corresponding to irreversible glucose oxidation, appear. For the Cu NB electrode, dramatic enhancement of the oxidation current can be observed between 0.2 - 0.7 V. For the NP electrode, the oxidation current increase starts only at 0.4 V. Amperometric sensing is a technique commonly applied for glucose detection.[2-16] It provides the response of oxidation current to analyte concentration variations. Figure 3.8B illustrates amperometric measurements of glucose by the nanostructured Cu electrodes (0.6 V in aerated 50 mM NaOH$_{(aq)}$). The NB electrode provides a much higher current response than the NP electrode does, as demonstrated in Figure 3.8C. A sensitivity of 79.8 μA/mM with a linear dependence (R^2 value, 0.998) of oxidation current to glucose concentration
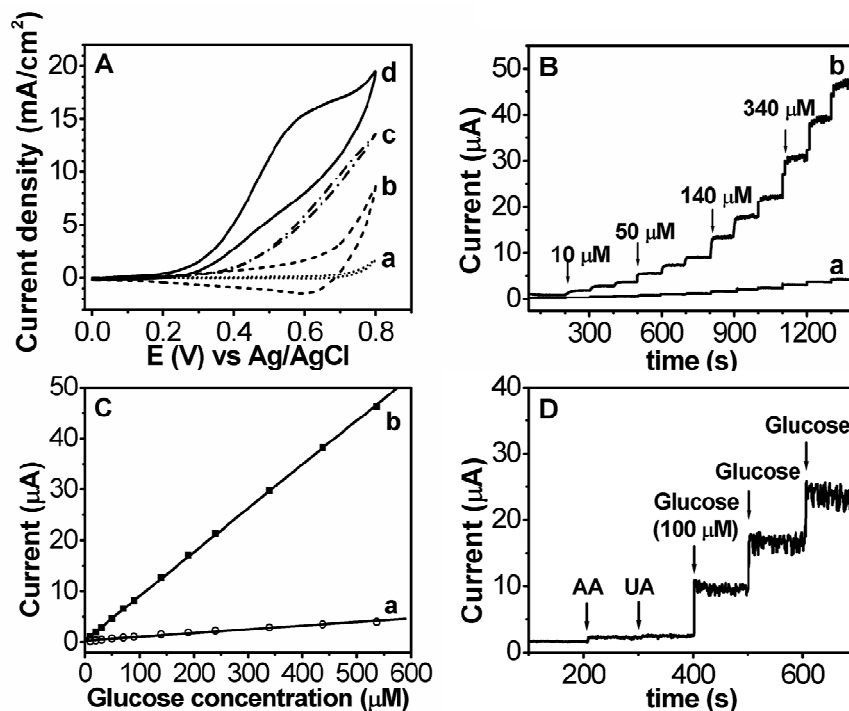
Figure 3.8. Electrochemical data of Cu electrodes in 50 mM NaOH at 50 mV/s. (A) CV diagram of (a) NP and (b) NB electrodes without glucose, and (c) NP and (d) NB electrodes in 0.1 M glucose; (B) amperometric responses (at 0.6 V) of (a) NP and (b) NB electrodes (0.018 cm^2) to successive additions of glucose; (C) current responses of (a) NP and (b) NB electrodes to glucose concentrations from the data in (B); (D) amperometric responses (at 0.6 V) of a NB electrode to interferences from ascorbic acid (AA, 10 µM) and uric acid (UA, 10 µM) prior to successive additions of glucose.

(10.0 µM - 1.13 mM) is observed for the NB electrode. The limit of detection (LOD) is 0.1 µM with a signal to noise ratio of 3. Performance of the NP electrode agrees with the reported data (sensitivity: 6.2 µA/mM; LOD: 0.96 µM).[14-15] Compared to other nanostructured electrodes reported previously, our Cu NB electrodes showed superior performance. Some literature examples, as listed in Table 3.1, are Cu NPs/CNT (sensitivity: 17.76 µA/mM; LOD: 0.2 µM), Pt NPs/CNT (sensitivity: 2.11 µA/mM; LOD: 0.5 µM) composite electrodes and Pt NTs electrodes (sensitivity: 7.58 µA/mM; LOD: 1.0 µM).[4,9,14]

Table 3.1 The comparison of the performance of nanostructured electrodes for glucose detection.

Electrode	Geometric area (cm^2)	Sensitivity (μA/mM)	LOD (μM)	Reference
Cu NBs	0.018	79.8	0.14	This study
Cu NPs	0.018	6.2	0.96	This study
Cu NPs/ MWCNT	0.07	17.76	0.21	*Anal. Biochem.* **2007**
Pt NPs/ SWCNT/ Enzyme	0.07	2.11	0.5	*Anal. Chem.* **2004**
Pt NTs	0.1256	7.58[a]	1.0	*Adv. Fun. Mater.* **2005**

[a] the data was calculated from conversion of specific sensitivity (μA/cm^{2}mM) producing real surface area of electrodes

In addition, the design and fabrication steps of our Cu NB electrodes are simple and straightforward while low-cost materials are employed. These are the other advantages relative to the reported enzymatic sensors and template-assisted nanoelectrodes.[2-7,9-11] In real physiological samples, interfering species such as L-ascorbic acid (AA) and uric acid (UA) normally co-exist with glucose. Their concentrations are about one-tenth of that of glucose levels. Amperometric responses of the NB electrode towards the addition of these two species (10 μM) followed by glucose (100 μM successively) were examined. As shown in Figure 3.8D, presence of AA and UA produces insignificant responses only, compared to the addition of glucose. The glucose response is still consistent with the calibration curve in Figure 3.8C, with a deviation of only 5%.

3.4 Conclusion

In conclusion, our results indicate that the Cu NB electrode can enhance electro-catalytic ability of glucose oxidation significantly. The high performance may be attributed to the large electrochemical surface area of the NBs and the exposed (111) belt surface planes.[34] Presence of better contacts between the NBs and the substrate may also show positive effects. Thus, the kinetically-controlled electro-oxidation of glucose is amplified and the response current is increased. We anticipate that these low-cost and easy to fabricate Cu NB electrodes will perform exceptionally in sensing glucose concentrations in real biological samples. Research is in progress.

3.5 References

1. See World Health Organization (WHO) website: http://www.who.int/en/

2. Clark, L.C.; Lyons, C. *Ann. N.Y. Acad. Sci.* **1962**, *102*, 29.

3. Zhao, H.T.; Ju, H. X. *Anal. Biochem.* **2006**, *350*, 138.

4. Hrapovic, S.; Liu, Y.; Male, K. B.; Luong, J. H. T. *Anal. Chem.* **2004**, *76*, 1083.

5. Forzani, E. S.; Zhang, H. Q.; Nagahara, L. A.; Amlani, I.; Tsui, R.; Tao, N. J. *Nano Lett.* **2004**, *4*, 1785.

6. Wen, X.; Xie, Y. T.; Wing, M.; Mak, C.; Cheung, K. Y.; Li, X. Y.; Renneberg, R.; Yang, S. *Langmuir* **2006**, *22*, 4836.

7. Lee, H.; Yoon, S. W.; Kim, E. J.; Park, J. *Nano Lett.* **2007**, *7*, 778.

8. Ye, J. S.; Wen, Y.; Zhang, W. D.; Gan, L. M.; Xu, G. Q.; Sheu, F. S. *Electrochem. Commun.* **2004**, *6*, 66.

9. Yuan, J. H.; Wang, K.; Xia, X. H. *Adv. Funct. Mater.* **2005**, *15*, 803.

10. Park, S.; Chung, T. D.; Kim, H. C. *Anal. Chem.* **2003**, *75*, 3046.

11. Song, Y. Y.; Zhang, D.; Gao, W.; Xia, X. H. *Chem. Eur. J.* **2005**, *11*, 2177.

12. Jena, B. K.; Raj, C. R. *Chem. Eur. J.* **2006**, *12*, 2702.

13. Wang, G.; Mantey, K.; Nayfeh, M. H.; Yau, S.-T. *Appl. Phys. Lett*. **2006**, *89*, 243901.

14. Kang, X.; Mai, Z.; Zou, X.-Y.; Cai, P.-X.; Mo, J.-Y. *Anal. Biochem.* **2007**, *363*, 143.

15. Zhao, J.; Wang, F.; Yu, J.; Hu, S. *Talanta* **2006**, *70*, 449.

16. Zhuang, Z. J.; Su, X. D.; Yuan, H. Y.; Sun, Q.; Xiao, D.; Choi, M. M. F. *Analyst* **2008**, *133*, 126.

17. Bai, J.; Qin, Y.; Jiang, C.; Qi, L. *Chem. Mater.* **2007**, *19*, 3367.

18. Sun, Y.; Mayers, B.; Xia, Y.-N. *Nano Lett.* **2003**, *3*, 675.

19. Zhang, J. L.; Du, J. M.; Han, B. X.; Liu, Z. M.; Jiang, T.; Zhang, Z. F. *Angew. Chem., Int. Ed.* **2006**, *45*, 1116.

20. Zhao, N.; Wei, Y.; Sun, N.; Chen, Q.; Bai, J.; Zhou, L.; Qin, Y.; Li, M.; Qi, L. *Langmuir* **2008**, *24*, 991.

21. Zhang, J.; Liu, H.; Wang, Z.; Ming, N. *Appl. Physics Lett.* **2007**, *91*, 133112.

22. Chen, Y.; Milenkovic, S.; Hassel, A. W. *Nano Lett.* **2008**, *8*, 737.

23. Liu, Z.; Li, S.; Yang, Y.; Peng, S.; Hu, Z.; Qian, Y. *Adv. Mater.* **2003**, *15*, 1946.

24. Huang, T.-K., Cheng, T.-H.;Yen, M.-Y.;Hsiao, W.-H.; Wang, L.-S. Chen, F.-R.; Kai, J.-J. Lee, C.-Y.; H.-T. Chiu *Langmuir* **2007**, *23*, 5722.

25. Wang, Z. L. *Adv. Mater.* **2003**, *15*, 432.

26. Pan, Z. W.; Dai, Z. R.; Wang, Z. L. *Science* **2001**, *291*, 1947.

27. Shi, W. S.; Peng, H. Y.; Wang, N.; Xu, C. P.; Li, L.; Lee, C. S.; Lee, S. T. *J. Am. Chem. Soc.* **2001**, *123*, 11095.

28. Ma, Y.; Qi, L.; Shen, W.; Ma, J. *Langmuir* **2005**, *21*, 6161.

29. Cao, X. B.; Xia, Y.; Zhang, S. Y.; Li, F. Q. *Adv. Mater.* **2004**, *16*, 649.

30. Mo, M.; Zeng, J.; Lin, X.; Yu, W.; Zhang, S.; Qian, Y. *Adv. Mater.* **2002**, *14*, 1658.

31. Zhang, M.; Wang, Z.; Xi, G.; Ma, D.; Zhang, R.; Qian, Y. *J. Cryst. Growth* **2004**, *268*, 215.

32. Law, M.; Sirbuly, D.; Johnson, J.; Goldberger, J.; Saykally, R.; Yang, P.-D. *Science* **2004**, *305*, 1269.

33. Zen, J.-M.; Hsu, C.-T.; Kumar, A. S.; Lyuu, H.-J.; Lin, K.-Y. *Analyst* **2004**, *129*, 841.

34. Takahashi, I.; Koga, O.; Hoshi, N.; Hori, Y. *J. Electroanal. Chem.* **2002**, *533*, 135.

Chapter 4

Growth of Pagoda-Topped Tetragonal Cu Nanopillar Arrays

4.1 Introduction

One-dimensional (1D) metal nanowires (NWs), nanorods (NRs), and nanobelts (NBs) have attracted considerable attentions because of their promising applications in future.[1-15] However, facile and controllable fabrication of free-standing metal NW arrays is still a difficult challenge. Hard templates with 1D channels, such as anodic aluminum oxide (AAO) and iontracked membranes, were often employed for high density 1D metal growths.[8-13] Hard template-free processes are rare. In some cases, penta-twinned Cu NWs grown upward on hard substrates by chemical vapor deposition (CVD) were reported.[14,15] These processes were rather complicated and relatively expensive equipments were needed. Recently, we have demonstrated that by using simple galvanic displacement reactions, novel nanostructures of Cu, Ag and Au can be grown directly on conducting substrates efficiently.[16-17] In these cases, morphology of the products were adjusted by suitable surfactants, acting as growth control agents. Here, we wish to report the growth and characterization of an unusual new type of 1D Cu in a form of pagoda-topped tetragonal nanopillar arrays, previously unknown in literature, by this route. In addition, our preliminary investigation demonstrates that the Cu nanopillars can emit electrons efficiently under applied electrical fields.

4.2 Experimental

4.2.1 Preparation of Tetragonal Cu Nanopillars

A summary of growth conditions of Cu nanopillars is listed in Table 4.1. The optimum growth condition (Pillar-3) is described below as a typical example.

Table 4.1 A summary of growth conditions of Cu nanopillars.

Sample	$CuCl_2$ (mM)	DTAC (mM)	Temperature (^{o}C)	Time (h)
Pillar-1	5	0.075	17	7
Pillar-2	5	0.3	17	7
Pillar-3	5	0.15	17	7
Pillar-4	5	0.15	17	1
Pillar-5	5	0.15	17	3
Pillar-6	5	0.15	17	12

A glass substrate ($5 \times 10 \times 1$ mm^3) was ultrasonically cleaned in alcohol and acetone for 10 min sequentially. The substrate was masked with Scotch tape to leave an exposed rectangular surface (1.5×4 mm^2). Then, a layer of Au with a thickness of 5 nm was deposited onto the substrate by DC sputtering (2.2 kV, 15 mA, 120 s). Finally, the tape mask was removed to offer the Au electrode. A piece of Al metal sheet ($1 \times 2 \times 0.5$ mm^3) was ultrasonically cleaned in alcohol (5 min), $H_3PO_{4(aq)}$ (Riedal-de Haen, 5%, 2 min), and finally, rinsed by deionized water. The Al slice was then attached to one side of the Au electrode by silver paste (Toyobo) and dried on a hot plate (353 K, 1 h). The whole glass substrate was immersed into a limpid aqueous solution (4 mL) containing $CuCl_2$ (5 mM, Strem) and dodecyltrimethylammonium chloride (DTAC)(0.15 mM, Fluka) In a glass vial at 290 K without stirring. The golden electrode turned black rapidly from its edge to the center within 2 min. As the reaction proceeded, it turned into dark red gradually. After a designated period of time (7 h), the substrate was removed and rinsed by deionized water and dried in a

desiccator.

4.2.2 Characterization

The deposited product layer was characterized by SEM (JEOL JSM-7401 at 15 kV), EDS (Oxford Link Pentafet), FETEM (JEOL JEM-2010F at 200 kV and JEOL JEM-4000EX), and XRD (Bruker AXS D8 Advance). Current-Voltage properties from field emission measurements were carried out using a needle-shaped anode with an effective tip to sample distance of 65 µm in a vacuum chamber at 4×10^{-6} torr at room temperature. A positive voltage swept up to 1 kV with a step of 50 V was applied to the anode using a Keithly 2410 power supply.

4.3 Results

4.3.1 SEM and EDS characterization

Figure 4.1a shows a field-emission scanning electron microscopic (SEM) image of Pillar-1. The product grew into a pine tree-like morphology in 0.075 mM DTAC. A detailed image shows that all stems and branches of the tree-like configuration displayed an analogous tetragonal structure, as shown in Figure 4.1b. Figure 4.1c shows a SEM image of Pillar-2. An enlarged image shows that tree-like products were not observed. Many large clusters were produced in 0.03 mM DTAC, as shown in Figure 4.1d.

Figure 4.2 shows that SEM images of Pillar-3 produced in 0.15 mM DTAC solution. Straight 1D NRs pointing randomly grow densely on the substrate, as shown in Figure 4.2a.
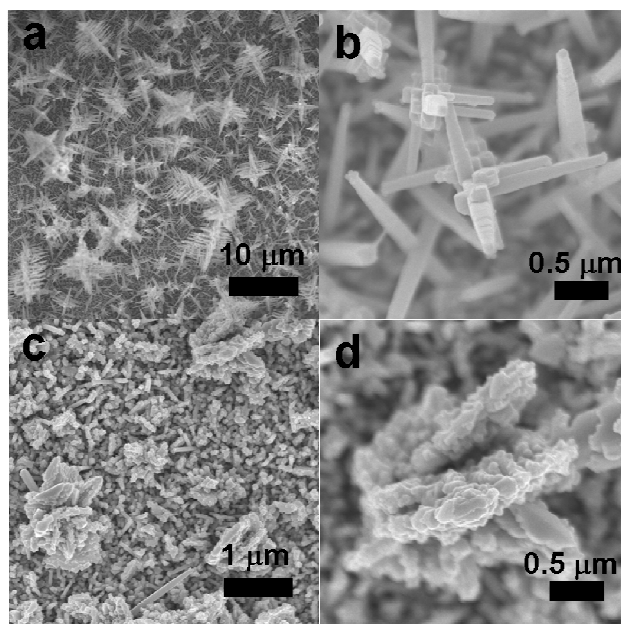
Figure 4.1 Low and high magnification SEM images of Cu nanostructures on Au/glass substrates at different DTAC concentrations at 7 h. (a), (b) 0.075 mM (Pillar-1) and (c), (d) 0.3 mM (Pillar-2).
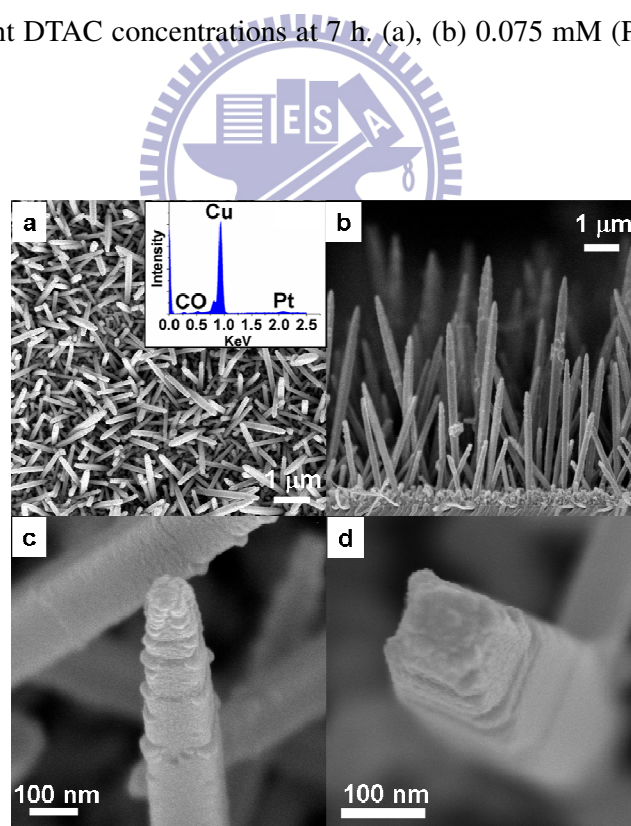

Figure 4.2 SEM images of Cu nanopillars (Pillar-3) on Au/glass. (a) Top view (inset: EDS), (b) side view, and (c) side view and (d) top view of a pagoda-shaped tip.

An energy dispersive spectrum (EDS, inset Figure 4.2a) confirms that the NRs are composed of Cu mainly. The Pt signal is due to a sputtered Pt thin layer for clear SEM observation. The C signal may originate from the surfactant while the tiny O signal is the consequence of surface oxidation of Cu during the sample preparation under atmosphere. Figure 4.2b shows a side view of the product on Au/glass. This displays an array of NRs aiming upward. The NRs are 1 – 6 μm long and 150 ± 25 nm wide. Some of the longest NRs show length-to-width aspect ratios close to 50. Between the array and the substrate, there is a layer (0.6 μm in thickness) of nanoparticles (NPs, 30 – 200 nm in size), presumably formed at the early growth stage. Figures 1c and 1d show enlarged views of a typical NR tip found in the array, revealing its four-side pagoda-like morphology. The pagoda has a height of 400 nm and a bottom perimeter of 600 nm. The images also suggest that the NR's main body has an apparent tetragonal geometry. This is confirmed by the observation of an idealized tetragonal-shaped NR with a flat top square face in the SEM images. Thus, we conclude that majority of the NRs has a tetragonal pillar-like main body with a pagoda-shaped tip. Consequently, we name this unique type of new structure "pagoda-topped tetragonal Cu nanopillar".

Figure 4.3 shows growth evolution of nanopillars at different growth time. Pillar-4 was prepared for 1 h. A layer of cube-like Cu NPs grew on the substrate, as shown in Figure 4.3a. Figure 4.3b shows that nananopillars with a length of up to 1 μm grew on the NP layer in Pillar-5 after 3 h. Based on experimental observation, the length of nanopillars increase gradually as growth time within 7 h. When growth time is elongated to 12 h, Pillar-6 were obtained. Figure 4.3c shows that pine tree-like dendrites were produced. This was also observed for the product grown in absence or deficiency of DTAC (Pillar-1).

4.3.2 XRD Analysis

XRD pattern of nanopillars grown on Au/glass is shown in Figure 4.4. The peaks at 2θ =
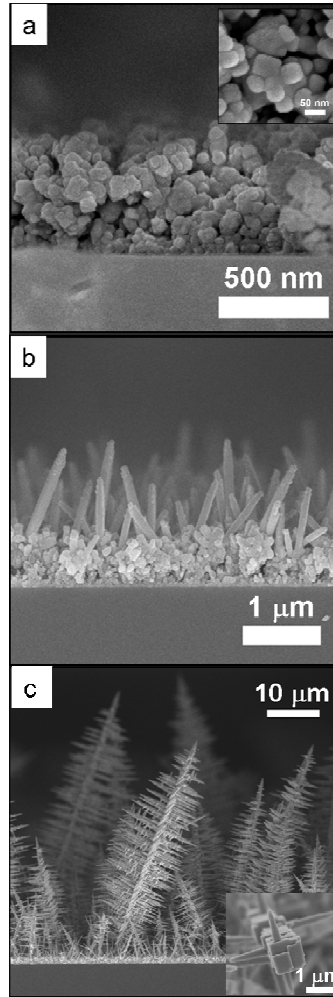
Figure 4.3 Side-view SEM images of Cu nanostructures on Au/glass substrates at different growing time. (a) 1 h (Pillar-4), (b) 3 h (Pillar-5), and (c) 12 h (Pillar-6). The insets show top view images enlarged.

43.0^o, 50.1^o, and 74.0^o are assigned to Cu (111), (200), and (220) reflections, respectively (JCPDF 89-2838). Lattice constant a is estimated to be 0.362 nm, is consistent with the reported value of Cu (JCPDF 89-2838). Reflections at $2\theta = 38.0^o$, and 43.8^o are from residual Ag paste after Al was removed (JCPDF 04-0783). The remaining peak at 54.0 are from a XRD holder. XRD patterns confirmed that the nanopillars are composed of a face-centered cubic (fcc) structure.
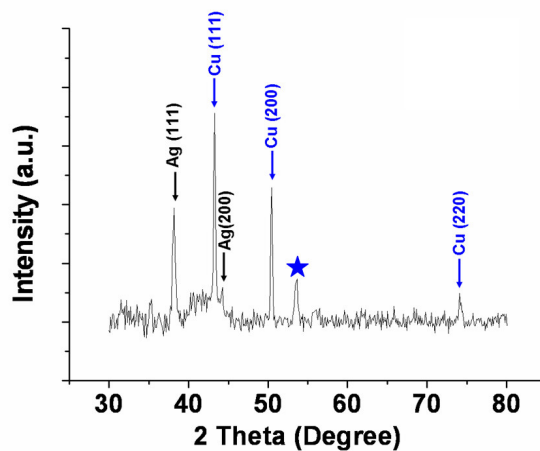
Figure 4.4 XRD of Cu nanopillars on Au/glass. Reflections of Ag were from residual Ag paste after Al was removed. (★: peaks from holder.).

4.3.3 TEM Characterization

Figure 4.5 shows a low magnification transmission electron microscopic (TEM) image of a representative nanopillar with an overall length of 3.6 μm. The regions selected from the tip, the body, and the root, as shown in Figure 4.5a, have side widths 100, 130, and130 nm, respectively. Their corresponding selected area electron diffraction (SAED) patterns are displayed in Figures 4.5b - d, respectively. All three images present identical square-shaped spot patterns, revealing the single crystalline nature of the nanopillar. The *d* spacing estimated from the spots closest to the beam center is 0.18 nm. This is consistent with the *d* spacing of Cu (200) planes (JCPDF 89-2838). Thus, the lattice parameter *a* is determined to be 0.36 nm, consistent with the reported value of fcc Cu. From the patterns, the crystallographic zone axis can be was corresponded to [001]. In addition to the spots of Cu, there are extra dim spots, as shown by the one pointed by an arrow in Figure 4.5b, indicating the presence of a tiny quantity of Cu_2O. From this set of spots, a *d* spacing of 0.25 nm is estimated and assigned to be the *d* spacing of Cu_2O (111) planes, 0.246 nm (JCPDF 78-2076). Figure 4.5e shows an enlarged image of the lower half of tip shown in

57
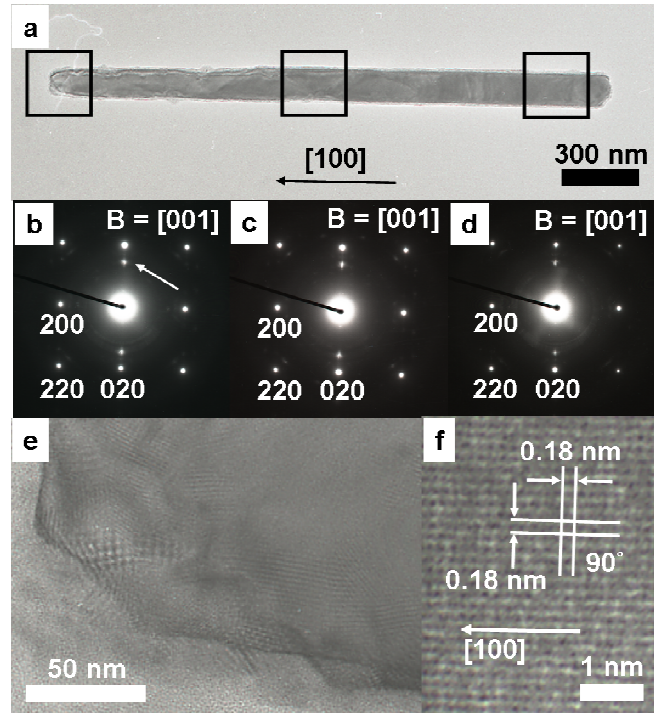
Figure 4.5 TEM studies of a Cu nanopillar. (a) Low magnification image; (b)-(d) SAED patterns of the rectangular marks in (a) indicating tip, middle, and bottom of the nanopillar (from left to right), respectively; (e) enlarged image of the lower half of the tip in (a); (f) HR image of the tip in (a).

Figure 4.5a. The complicated patterns and Moiré fringes are the result of uneven side walls of the pagoda shaped structure, as indicated in Figures 4.2c and d. Figure 4.5f shows a high-resolution TEM (HRTEM) image of the tip. The fringes are spaced 0.180 nm apart. These are consistent with the *d* spacing of Cu {200} planes (JCPDF 89-2838). The dihedral angle of 90° is also consistent with the theoretical value of Cu. Using the information discussed, growth direction of the nanopillars is determined to be along [100] while the four side walls are bounded by {100} planes.

4.3.4 Proposed Growth Mechanism

In Scheme 4.1, the overall growth steps are illustrated to account for the deposition of
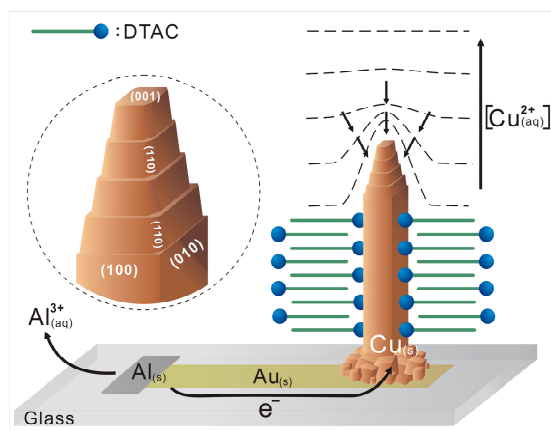
Scheme 4.1 Proposed growth mechanism of pagoda-topped tetragonal Cu nanopillars on Au/glass electrode. For clarity, only two side faces of the nanopillar are shown to be covered by DTAC.

pagoda-topped nanopillar. We attribute the growth of these unusual structures to the following reasons. First of all, the over all reduction of $Cu^{2+}_{(aq)}$ by $Al_{(s)}$ to form $Cu_{(s)}$ is thermodynamically favored, as suggested by the equation $3\ Cu^{2+}_{(aq)} + 2\ Al_{(s)} \rightarrow 3\ Cu_{(s)} + 2\ Al^{3+}_{(aq)}$, $E_0 = 2.00$ V.[18] This is especially favored at the initial growth stage. In the reaction, a layer of cube-like Cu NPs grew on the substrate after 1h. Apparently, $Cu^{2+}_{(aq)}$ ions near the electrode surface were reduced rapidly to deposit these NPs and served as the seeds of growth of the nanopillars. Secondly, diffusion limited conditions in electrochemical deposition system is important for anisotropic growths.[19] As the $Cu^{2+}_{(aq)}$ ion concentration near the electrode surface depleted, a concentration gradient of the ion was formed. This diffusion layer would favor anisotropic growth of the crystals. Finally, the presence of an adequate amount of DTAC is necessary. It probably acted as a capping reagent to assist shape control of the crystals. It is likely that the surfactant molecules self-assembled into a bilayer structure and co-adsorbed selectively on Cu {100} crystal planes to confine the branching growths.[1,16-17] In absence or deficiency of DTAC, the product grew into a pine tree-like morphology. This was also observed for the product grown at an extended

deposition time. All stems and branches of the tree-like configuration also displayed an analogous tetragonal structure closely related to the nanopillars. Clearly, capping of the DTAC surfactant molecules on {100} stabilized the facets and reduced further extrusion of branches from the stems. On the other hand, the nanopillar tip with the step-edge structure, which was near the bottom of the diffusion layer, could expose more active growth sites and allow more $Cu^{2+}_{(aq)}$ reduction on them for further nanopillar extension.[20] When near perfect {100} side facets were formed, DTAC would passivate them and confine transverse growth. When excess DTAC was added, large clusters were produced. Obviously, too much DTAC suppressed the anisotropic crystal growth condition because the direct galvanic displacement reaction was carried out at near equilibrium condition. This caused isotropic growth of polyhedron or sphere shaped crystals.[19]

4.3.5 Field Emission Properties

Because of their novel morphology, field emission (FE) properties of the pagoda-topped nanopillar arrays were investigated. For a typical sample, Figure 4.6 shows that the current density (J) of the emitted electrons increases dramatically over an electric field (E) threshold, the turn-on E, E_0. At E_0 of 12.4 V µm^{-1}, the J value is observed to be 10 µA cm^{-2}. The inset shows a plot of ln(J/E^2) versus 1/E. For 1/E between 0.06 and 0.15 µm V^{-1}, a straight line is observed. This indicates that the field emission character follows the model described by Fowler–Nordheim (FN) equation $J = A(\beta^2 E^2/\Phi)\exp(-B\Phi^{3/2}/\beta E)$.[21] In the equation, in addition to J and E mentioned above, Φ is the work function of Cu (4.47 eV), and A and B are constants, 1.56 × 10^{-10} (A V^{-2} eV) and 6.83 × 10^3 (V eV$^{-3/2}$ µm^{-1}), respectively.[14] β is field enhancement factor, a general parameter describing emitter performance. β is dependent on geometry and morphology of the nanostructure, crystal structure of the material, and density of the emitting points. Here, β is calculated to be 713.[14,21] In contrast, a layer of cube-like Cu NPs deposited at 1 h, does not show
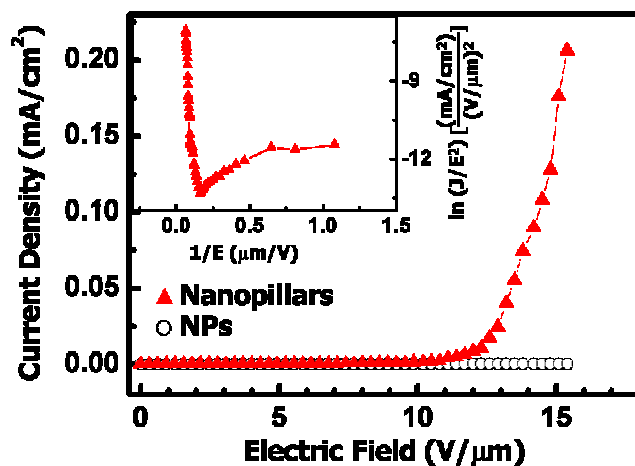
Figure 4.6 Emission current density as a function of applied electric field on Cu nanopillars (Pillar-3) and NPs (Pillar-4) (inset: corresponding F-N plots).

significant J within the field applied. With their high aspect ratios and unique pagoda-shaped tips, it is not a surprise that the nanopillars can extrude electrons much more efficiently than the NPs. In addition, β of the Cu nanopillars is superior to those of the other 1D Cu nanostructures reported previously, such as the NWs grown by hard-template assisted and CVD processes, 245 and 443 respectively.[13,15]

4.4 Conclusion

In conclusion, we have achieved a simple process to grow of arrays of pagoda-topped tetragonal Cu nanopillars with {100} side faces in this study. Growth time and DTAC concentration affect the product morphology significantly. FE measurement shows that the Cu nanopillars can emit electrons under relatively low electric field strength. We anticipate that this novel material could be employed for interesting nanodevice applications in the future.

4.5 References

1. Murphy, C. J.; Sau, T. K.; Gole, A. M.; Orendorff, C. J.; Gao, J.; Gou, L.; Hunyadi, S. E.; Li, T. *J. Phys. Chem. B* **2005**, *109*, 13857.

2. Nikoobakht, B.; El-Sayed, M. A. *J. Phys. Chem. A* **2003**, *107*, 3372.

3. Grand, J.; de la Chapelle, M. L.; Bijeon, J. L.; Adam, P. M.; Vial, A.; Royer, P. *Phys. Rev. B* **2005**, *72*, 33407.

4. Hernandez, J.; Solla-Gullon, J.; Herrero, E.; Aldaz, A.; Feliu, J. M. *J. Phys. Chem. B* **2005**, *109*, 12651.

5. Langford, R. M.; Wang, T. X.; Thornton, M.; Heidelberg, A.; Sheridan, J. G.; Blau, W.; Leahy, R. *J. Vac. Sci. Technol. B* **2006**, *24*, 2306.

6. Hsia, C.-H.; Yen, M.-Y.; Lin, C.-C.; Chiu, H.-T.; Lee, C.-Y. *J. Am. Chem. Soc.* **2003**, *125*, 9940.

7. Yen, M.-Y.; Chiu, C.-W.; Hsia, C.-H.; Chen, F.-R.; Kai, J.-J.; Lee, C.-Y.; Chiu, H.-T. *Adv. Mater.* **2003**, *15*, 235.

8. Choi, J.; Sauer, G.; Goring, P.; Nielsch, K.; Wehrspohn, R. B.; Gosele, U. *J. Mater. Chem.* **2003**, *13*, 1100.

9. Dobrev, D.; Yao, H. J.; Sun, Y. M.; Hou, M. D.; Mo, D.; Wang, Z. G.; Neumann, R. *Nanotechnology* **2006**, *17*, 1922.

10. Li, N.; Li, X.; Yin, X.; Wang, W.; Qiu, S. *Solid State Commun.* **2004**, *132*, 841.

11. Choi, J.; Sauer, G.; Nielsch, K.; Wehrspohn, R. B.; Gosele, U. *Chem. Mater.* **2003**, *15*, 776.

12. Dangwal, A.; Pandey, C. S.; Muller, G.; Karim, S.; Cornelius, T. W.; Trautmann, C. *Appl. Phys. Lett.* **2008**, *92*, 3.

13. Maurer, F.; Dangwal, A.; Lysenkov, D.; Muller, G.; Toimil-Molares, M. E.; Trautmann, C.; Brotz, J.; Fuess, H. *Nucl. Instrum. Meth. B* **2006**, *245*, 337.

14. Wang, J.-H.; Yang, T.-H.; Wu, W.-W.; Chen, L.-J.; Chen, C.-H.; Chu, C.-J. *Nanotechnology* **2006**, *17*, 719.

15. Kim, C.; Gu, W.; Briceno, M.; Robertson, I. M.; Choi, H.; Kim, K. K. *Adv. Mater.* **2008**, *20*, 1859.

16. Huang, T. K.; Cheng, T. H.; Yen, M. Y.; Hsiao, W. H.; Wang, L. S.; Chen, F. R.; Kai, J. J.; Lee, C. Y.; Chiu, H. T. *Langmuir* **2007**, *23*, 5722.

17. Huang, T.-K.; Chen, Y.-C.; Ko, H.-C.; Huang, H.-W.; Wang, C.-H.; Lin, H.-K.; Chen, F.-R.; Kai, J.-J.; Lee, C.-Y.; Chiu, H.-T. *Langmuir* **2008**, *24*, 5647.

18. Bard, A. J.; Faulkner, L. R., *Electrochemical Methods: Fundamentals and Applications*, John Wiley & Sons, New York **1980**.

19. Fukami, K.; Nakanishi, S.; Yamasaki, H.; Tada, T.; Sonoda, K.; Kamikawa, N.; Tsuji, N.; Sakaguchi, H.; Nakato, Y. *J. Phys. Chem. C* **2007**, *111*, 1150.

20. Walter, E. C.; Murray, B. J.; Favier, F.; Kaltenpoth, G.; Grunze, M.; Penner, R. M. *J. Phys. Chem. B* **2002**, *106*, 11407.

21. Fowler, R. H.; Nordheim, L. W. *Proc. R. Soc. A* **1928**, *119*, 173.

Chapter 5

Field Emission Properties of Gold Nanostructures Grown Directly on Silicon

5.1 Introduction

The field emission of electrons is a quantum-mechanical phenomenon, as a tunneling process across the energy barrier between the vacuum and the emitter. One-dimensional (1D) nanomaterials have been demonstrated to be induced several orders of magnitude of an external applied field due to their characteristics of the small tip and high aspect ratio.[1-5] In FE simulation, metal nanowires (NWs) are thought to be an excellent FE materials.[6] However, there are much few related reports. The key issue is that fabrication of NW arrays is crucial. The template-assisted approach, such as anodic aluminum oxide (AAO) and ion track membrane, is a known method.[7-9] Recently, chemical vapor deposition (CVD) is employed to grow free-standing Cu NWs for the FE device.[10,11] Until to now, growth and FE properties of 1D Au nanostructures on hard substrates without hard templates are less reported. As mentioned in Chapter 2-4, the electrochemical methods provided a successful approach to grow Cu nanobelts and nanopillars on electrodes. In this article, we present that a facile galvanic reduction to grow directly Au nanothorns and nanourchins on Si. Their shape-depend FE performance will be explored.

5.2 Experimental

A summary of growth conditions of Au nanostructures is listed in Table 5.1. Growth of Au nanourchins by galvanic reduction of $HAuCl_{4(aq)}$ by $Sn_{(s)}$ in the presence of CTAC and $NaNO_3$ (Urchin-18h) is described below as a typical example.

Table 5.1 A summary of growth conditions of Au nanostructures.

Sample	HAuCl$_4$ (mM)	CTAC (mM)	NaNO$_3$ (mM)	Time (h)	Temperature (^{o}C)
Thorn	5	0	20	18	30
Urchin-6h	5	9	20	6	30
Urchin-12h	5	9	20	12	30
Urchin-18h	5	9	20	18	30

5.2.1 Pre-treatment of Silicon

A n-type Si(100) wafer (TSR High Purity Si) was pre-roughened by a electroless etching process to enhance Au nucleation. After cleaned with acetone, the Si substrate, cut into 0.5 cm × 0.5 cm in size, was immersed into a Teflon bottle containing an etching solution, which was a mixture of 0.07 g AgNO$_3$ (Fisher), 2 mL of 48 % w.t. HF (Merck) and 10 mL deionized water for 5 min. After the etching step, the substrate was washed with concentrated HNO$_3$ (J. T. Baker) and followed by deionized water to remove Ag precipitates formed in the etching process. Finally, the pre-roughened Si was dried under a N$_2$ stream.

5.2.2 Fabrication of Sn-pasted Silicon

A piece of Sn metal (99.998%, Aldrich), used as the reducing metal, was pasted on the backside of the pre-roughened Si substrate by Ag glue (Toyobo). Then, the combined piece was dried in the oven at 383 K for 1 h.

5.2.3 Growth of Au Nanourchins

In a glass vial, a mixed growth solution containing HAuCl$_{4(aq)}$ (5 mM, SHOWA), CTAC$_{(aq)}$

(9 mM, Taiwan Surfactant) and $NaNO_{3(aq)}$ (20 mM, Shimakyu's Pure Chemicals) was prepared. It turned yellowish cloudy after mixing. Then, the Sn-pasted Si was immersed into the growth solution (4 mL). The reaction was controlled at 303 K for 18 h without stirring. Gradually, the solution near the wafer turned pink and the Si surface became golden. The final sample specimen was removed from the solution, rinsed with deionized water. and then dried under a N_2 stream.

5.2.4 Characterization

The samples were investigated by the following instruments: SEM (Hitachi S-4000 at 25 kV and JEOL JSM-6330F at 15 kV), EDS (Oxford Link Pentafet), TEM (JEOL JEM-2010F at 200 kV and JEOL JEM-4000EX), and XRD (Bruker AXS D8 Advance). Current-Voltage properties from field emission measurements were carried out using a needle-shaped anode with an effective tip to sample distance of 65 μm in a vacuum chamber at 4×10^{-6} torr at room temperature. A positive voltage swept up to 1 kV with a step of 50 V was applied to the anode using a Keithly 2410 power supply.

5.3 Result

5.3.1 SEM characterization

Sample Thorn was obtained by reduction of $HAuCl_4$ by Sn in the presence of only $NaNO_3$. After reaction, growth of a golden layer on the Si surface was observed. SEM images of Sample Thorn are shown in Figure 5.1. Figure 5.1A depicts that a high density of nanothorns with a length of 1-2 μm grow up on roughened Si. The width is about 0.5 μm near the base. A high magnification SEM image of nanothorns, as shown in Figure 5.1B, shows a pyramidal shape of a nanothorn.
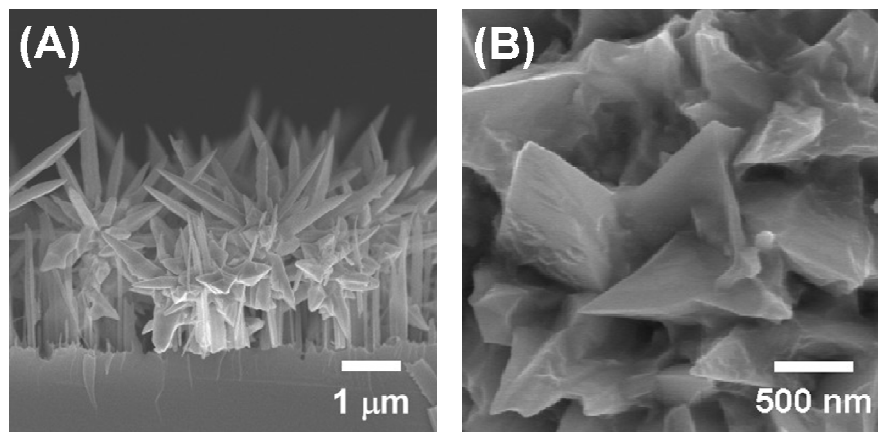
Figure 5.1. (A) Side-view and (B) top-view SEM images of Au nanothorns grown on Si.

Sample Urchin-6h, Urchin-12h, and Urchin-18h were prepared in an aqueous solution of both CTAC and $NaNO_3$ at three different growth time. Figure 5.2A shows SEM image of Urchin-6h at the early growth stage. The 2 μm diameter nuclei deposit dispersively on Si. An enlarged view of a nucleus shows that many nanosized pins protruded on the nucleus, as shown in Figure 5.2B. Each pin has a length of less than 200 nm. Figure 5.2C shows SEM image of Urchin-12h grown at 12 h. The density and dimension of nuclei are similar to Urchin-6h. Especially, a detailed image, as shown in Figure 5.2D, points out that a rod-like nanostructure is evolved from a small pin in Figure 5.2B. The diameter and length is about 100 nm and up to 500 nm, respectively. Because they have urchin-like nanostructures, we name gold nanourchins. When elongating growth time to 18 h, SEM images of Urchin-18h show multiple- and long- needle nanourchins, as shown in Figure 5.2E. Figure 5.2F shows that the protruding needles are on top of a nuclear particle. Each needle is like a straight nanowire, has a diameter of about 100 nm and a length of up to 3 μm.

Figure 5.3 shows an apparent pentagonal cross-section of short Au nanowires protruded on a nanourchin. This agrees well with the penta-twinned NW structure characterized by TEM studies in our previous report.[12]
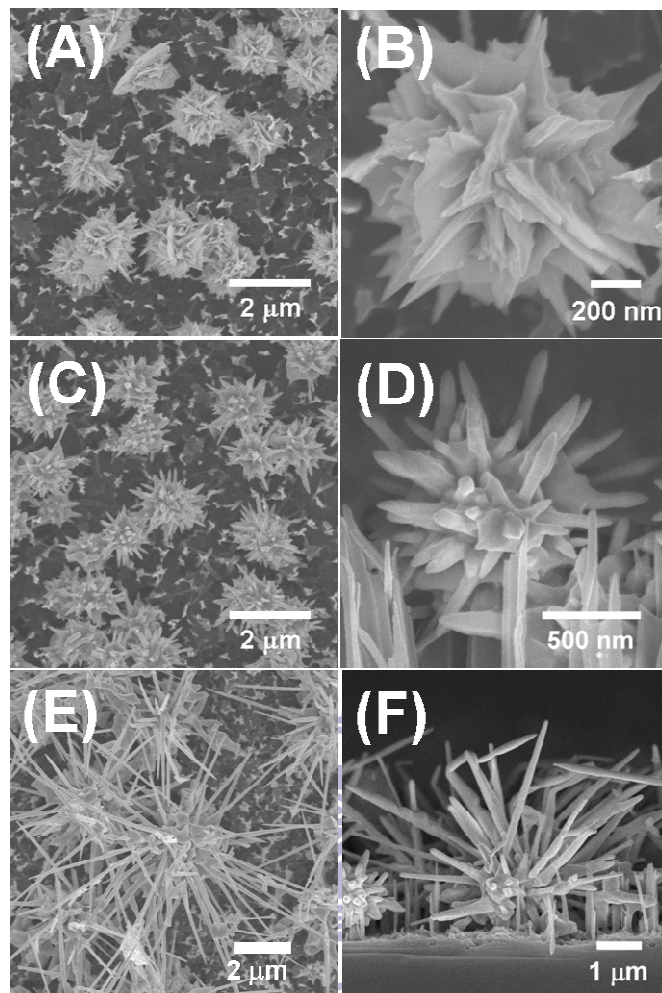
Figure 5.2. SEM images of Au nanourchins grown on pre-roughened Si at different growth time. (A)-(B) 6 h, (C)-(D) 12 h, and (E)-(F) 18 h.
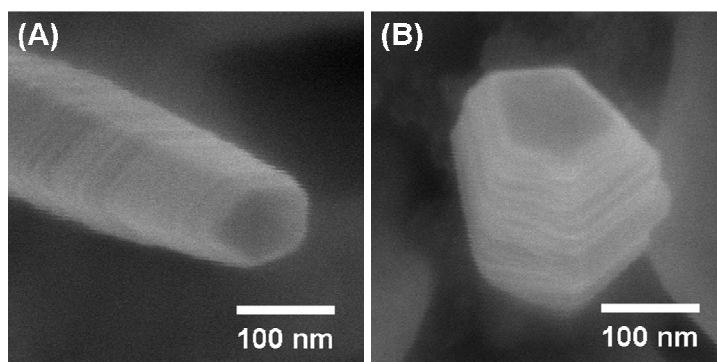

Figure 5.3. High Magnification SEM images of Au nanowires on nanourchins showing a pentagonal cross-section and a step structure on the side wall.

5.3.2 XRD analysis

Figure 5.4 shows XRD pattern of Thorn. The peaks at $2\theta = 38.1°$, $44.3°$, and $64.5°$ are assigned to Au (111), (200), and (220) reflections, respectively (JCPDF 89-3697). Lattice constant a is estimated to be 0.408 nm, close to the reported value, 0.4079 nm of Au (JCPDF 89-3697). This XRD study suggested that nanothorns consist of fcc Au.
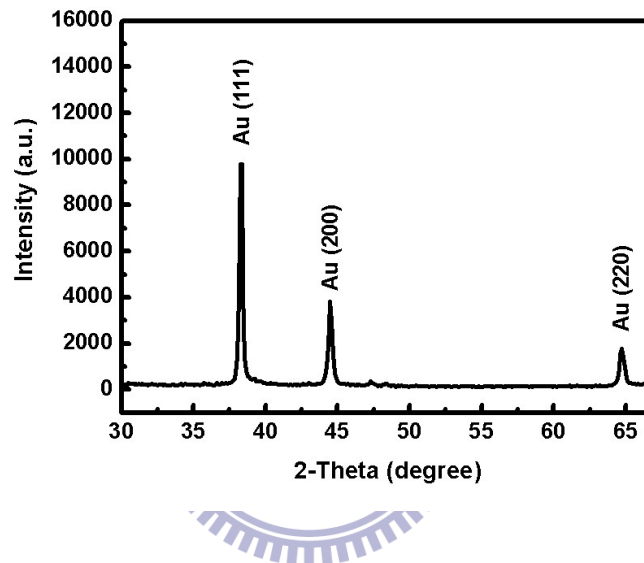
Figure 5.4 XRD of Au nanothorns grown on Si

5.3.3 FE Properties

Because of their novel morphology and direct growth on Si, field emission (FE) properties of Au nanothorns and nanourchins were investigated. The FE properties and the corresponding Fowler-Nordheim (F-N) plot are illustrated in Figure 5.5A and 5.5B, respectively. The turn-on field E_0 was designated as the interceptions of straight lines extrapolated from the low-field and high-field segments of the F-N plots. Thorn, Urchin-12h, and Urchin-18h show E_0 of 13.3, 10.2, and 6.3 Vμm^{-1}, respectively.
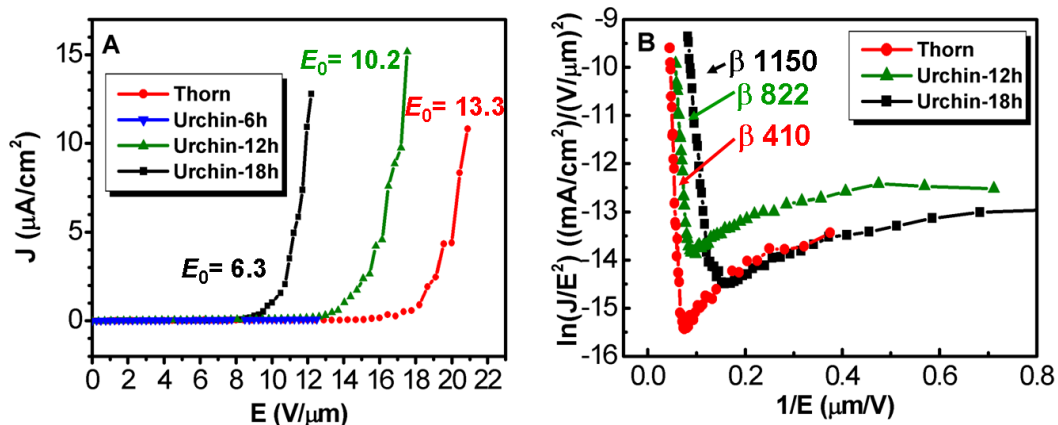
Figure 5.5 (A) Emission current density as a function of applied electric field (*J-E* plots) on Au nanostructures; (B) corresponding Fowler-Nordheim (F-N) plots.

Above this field strength, the emission current density increases dramatically. F-N plots of $\ln(J/E^2)$ versus $1/E$ observe a straight line in the high field. This indicates that the field emission character follows the model described by Fowler–Nordheim (FN) equation $J = A(\beta^2 E^2/\Phi)\exp(-B\Phi^{3/2}/\beta E)$.[13] In the equation, in addition to *J* and *E* mentioned above, Φ is the work function of Au (5.00 eV), *A* and *B* are constants, 1.56×10^{-10} (A V^{-2} eV) and 6.83×10^3 (V eV$^{-3/2}$ μm^{-1}), respectively.[7] β is field enhancement factor, a general parameter describing emitter performance. β is dependent on geometry and morphology of the nanostructure, crystal structure of the material, and density of the emitting points. Here, β of Thorn, Urchin-12h, and Urchin-18h are calculated to be 410, 822, and 1150.

In contrast, Urchin-6h does not show significant *J* within the *E* applied. This suggests that nanothorn and nanourchins with nanorods and nanowires exhibit the FE performace. Especially, nanowires with higher aspect ratio can extrude electrons much more efficiently. In addition, β of the Au nanourchins grown at 18h is superior to those of the other 1D Au and Cu nanostructures reported previously, such as the NWs grown by hard-template assisted and CVD processes, 632 and 443 respectively.[7, 10]

5.4 Conclusion

In conclusion, a simple process to grow of Au nanothorns and nanourchins on Si is achieved in this study. Growth time and additives affect the product morphology significantly. FE measurement shows that the Au nanothorns and nanourchins display a FE properties. Especially, nanourchin grown at 18 h can emit electrons under relatively low electric field strength. We anticipate that this novel material could be employed for interesting nanodevice applications in the future.

5.5 References

1. Choi, W. B.; Chung, D. S.; Kang, J. H.; Kim, H. Y.; Jin, Y. W.; Han, I. T.; Lee, Y. H.; Jung, J. E.; Lee, N. S.; Park, G. S., *Appl. Phys. Lett.* **1999**, *75*, 3129.

2. Fang, X.; Bando, Y.; Ye, C.; Shen, G.; Gautam, U. K.; Tang, C.; Golberg, D., *Chem. Comm.* **2007,** *2007*, 4093.

3. Tzeng, Y. F.; Lee, Y. C.; Lee, C. Y.; Lin, I. N.; Chiu, H. T., *Appl. Phys. Lett.* **2007,** *91*, 063117.

4. Lin, H. K.; Tzeng, Y. F.; Wang, C. H.; Tai, N. H.; Lin, I. N.; Lee, C. Y.; Chiu, H. T., *Chem. Mater.* **2008**, *20*, 2429.

5. Wang, C. H.; Lin, H. K.; Ke, T. Y.; Palathinkal, T. J.; Tai, N. H.; Lin, I. N.; Lee, C. Y.; Chiu, H. T., *Chem. Mater.* **2007,** *19*, 3956.

6. Lee, C. K.; Lee, B.; Ihm, J.; Han, S., *Nanotechnology* **2007,** *18*, 5.

7. Dangwal, A.; Pandey, C. S.; Muller, G.; Karim, S.; Cornelius, T. W.; Trautmann, C., *Appl. Phys. Lett.* **2008,** *92*, 063115-3.

8. Maurer, F.; Dangwal, A.; Lysenkov, D.; Muller, G.; Toimil-Molares, M. E.; Trautmann, C.; Brotz, J.; Fuess, H., *Nuclear Inst. and Methods in Physics Research, B* **2006,** *245*, 337-341.

9. Davydov, D. N.; Sattari, P. A.; AlMawlawi, D.; Osika, A.; Haslett, T. L.; Moskovits, M., *J. Appl. Phys.* **1999,** *86*, 3983.

10. Kim, C.; Gu, W. H.; Briceno, M.; Robertson, I. M.; Choi, H.; Kim, K., *Adv. Mater.* **2008,** *20*, 1859.

11. Wang, J.-H.; Yang, T.-H.; Wu, W.-W.; Chen, L.-J.; Chen, C.-H.; Chu, C.-J., *Nanotechnology* **2006,** *17*, 719.

12. Huang, T. K.; Chen, Y. C.; Ko, H. C.; Huang, H. W.; Wang, C. H.; Lin, H. K.; Chen, F. R.; Kai, J. J.; Lee, C. Y.; Chiu, H. T., *Langmuir* **2008,** *24*, 5647.

13. Fowler, R. H.; Nordheim, L. W., *Proc. R. Soc. A* **1928,** *119*, 173.

Chapter 6

Conclusions

In this thesis, we employed surfactant assisted electrochemical methods to grow Cu and Au nanostructures on hard substrates. Galvanic reduction of $CuCl_{2(aq)}$ by $Al_{(s)}$ and $HAuCl_{4(aq)}$ by $Sn_{(s)}$ can grow Cu nanobelts, pagoda-topped tetragonal nanopillar arrays, Au nanothorns, and nanourchins. Cu NBs can also be grown on carbon electrode by electrochemical deposition in $CuCl_{2(aq)}$ aqueous solution. Kinetic control dominates formation of these novel nanocrystal. Diffusion limited condition formed in the electrochemical growth process is thought to cause anisotropic dendridic crystal. Surfactants, such as CTAC and DTAC play a role of capping reagent to confine and stabilize crystal growth to form the non-branching 1D nanostructures. Moreover, the environment of NO_3^- and Cl^- may provide a selective etching ability on a certain crystal facets. These are all the key factors controlling evolution of 1D nanocrystal in the electrochemical system.

We have also explored the properties and application of these unique nanostructures. Cu NB electrodes exhibit a large surface area and high electro-catalytic ability of glucose. In amperometric sensing of glucose, Cu NB electrode possesses high sensitivity and low detection limit compared to the other electrodes reported previously. A array of free-standing Cu nanopillars grow upward on Au/glass. The characteristics of a straight structure, high aspect ratio, and pointed tip of nanopillars lead to an excellent FE property with high emission current and large β. Au nanothorns and nanourchins are composed of radially protruding 1D nanostructures on Si. The comparison of their FE measurements reveal that Au nanourchin grown at 18 h exhibits a superior FE performance. It suggests that

electron emitting efficiency is promoted as the aspect ratio increases.

We conclude that the surfactant assisted electrochemical method is an effective route to grow distinctive Cu and Au nanostructure. This method also provides a straightforward way to integrate nanomaterials into nanodevices. It can be anticipated that more unusual nanostructures and high-efficiency minimized devices will be developed by this method in future.